SANDIA REPORT

SAND2013-8163
Unlimited Release
September, 2013

Improved Flywheel Materials: Characterization of Nanofiber Modified Flywheel Test Specimen.

Timothy J. Boyle, Nelson Bell, Mark Ehlen, Ben Anderson, William Miller

Prepared by
Sandia National Laboratories
Albuquerque, New Mexico 87185 and Livermore, California 94550

Sandia National Laboratories is a multi-program laboratory managed and operated by Sandia Corporation, a wholly owned subsidiary of Lockheed Martin Corporation, for the U.S. Department of Energy's National Nuclear Security Administration under contract DE-AC04-94AL85000.

Issued by Sandia National Laboratories, operated for the United **S**tates Department of Energy by Sandia Corporation.

Available to DOE and DOE contractors from
U.S. Department of Energy
Office of Scientific and Technical Information
P.O. Box 62
Oak Ridge, TN 37831

Telephone: (865) 576-8401
Facsimile: (865) 576-5728
E-Mail: reports@adonis.osti.gov
Online ordering: http://www.osti.gov/bridge

Available to the public from
U.S. Department of Commerce
National Technical Information Service
5285 Port Royal Rd.
Springfield, VA 22161

Telephone: (800) 553-6847
Facsimile: (703) 605-6900
E-Mail: orders@ntis.fedworld.gov
Online order: http://www.ntis.gov/help/ordermethods.asp?loc=7-4-0#online

SAND2013-8163
Unlimited Release
September 2013

Improved Flywheel Materials: Characterization of Nanofiber Modified Flywheel Test Specimen

Timothy J. Boyle
Advanced Materials Laboratory

Nelson Bell
Electrical, Optical and Nano

Mark Ehlen
Policy and Decision Analytics

Ben Anderson
Organic Materials Science

William Miller
Packaging & Polymer Processing

Sandia National Laboratories
P.O. Box 5800
Albuquerque, New Mexico 87185-MS1349

Abstract

As alternative energy generating devices (i.e., solar, wind, etc) are added onto the electrical energy grid (AC grid), irregularities in the available electricity due to natural occurrences (i.e., clouds reducing solar input or wind burst increasing wind powered turbines) will be dramatically increased. Due to their almost instantaneous response, modern flywheel-based energy storage devices can act a mechanical mechanism to regulate the AC grid; however, improved spin speeds will be required to meet the necessary energy levels to balance these 'green' energy variances. Focusing on composite flywheels, we have investigated methods for improving the spin speeds based on materials needs. The so-called composite flywheels are composed of carbon fiber (C-fiber), glass fiber, and a 'glue' (resin) to hold them together. For this effort, we have focused on the addition of fillers to the resin in order to improve its properties. Based on the high loads required for standard meso-sized fillers, this project investigated the utility of ceramic nanofillers since they can be added at very low load levels due to their high surface area. The impact that TiO_2 nanowires had on the final strength of the flywheel material was determined by a 'three-point-bend' test. The results of the introduction of nanomaterials demonstrated an increase in 'strength' of the flywheel's C-fiber-resin moiety, with an upper limit of a 30% increase being reported. An analysis of the economic impact concerning the utilization of the nanowires was undertaken and after accounting for new-technology and additional production costs, return on improved-nanocomposite investment was approximated at 4-6% per year over the 20-year expected service life. Further, it was determined based on the 30% improvement in strength, this change may enable a 20-30% reduction in flywheel energy storage cost ($/kW-h).

Contents

NOMENCLATURE

AML	Advanced Materials Laboratory
DOE	Department of Energy
SNL	Sandia National Laboratories

1. INTRODUCTION

The network of interconnected lines for transmitting and distributing electrical energy in the United States is often referred to as the 'power grid'. Most of the three major grids in the US [Western Interconnection, Eastern Interconnection, and the Electrical Reliability Council of Texas (ERCOT)] employ high-voltage, three-phase, alternating currents and thus this network is referred to as the AC-grid. In order for a safe and stable AC grid, the supply and demand of electricity must be exactly regulated at 60 Hz. However, due to the inconsistent load placed by consumers, significant variations (i.e., surplus and deficits) of electricity occurs. Traditionally, this is accounted for by gas powered generators, which are inefficient, wasteful, cause green house emissions, and cause significant wear and tear on the equipment. Further, as non-traditional sources of electricity (i.e., wind or solar) become a larger part of the AC grid, significant issues concerning energy regulation will occur due to the inconsistent energy produced using these 'green' methods. For instance, for wind power gusts due to storms or other weather phenomenon will cause spikes in energy production, while clouds will cause unpredictable times of reduced electrical production for solar energy. This will place significant hardships on the regulation of the AC grid requiring faster responses than currently being explored.

One technology that can assist in storing the excess energy and delivering/collecting electricity instantly upon demand is flywheels. Flywheels are mechanical batteries that have been around since the Neolithic era. In general, flywheels store rotational energy by spinning a wheel that have a significant moment of inertia. In the 1800s, flywheels were employed as a means to regulate electrical energy for industrial applications (Figure 1) and were traditionally

large, heavy, metal devices, which limited their rotation speeds to a few thousand revolutions per minute (rpm).

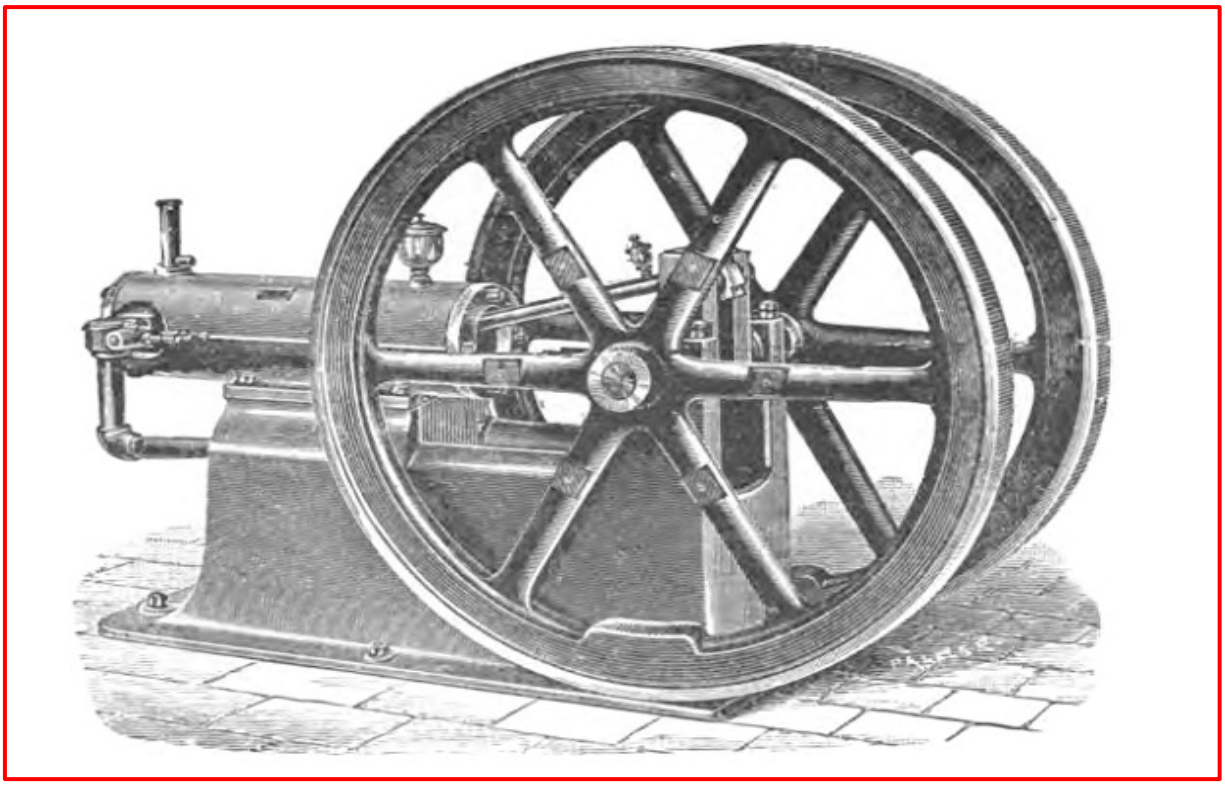

Figure 1. 1898 illustration of a White and Middleton stationary engine; note the large twin flywheels.

In contrast, modern flywheels have a variety of compositions but the commercially used composite flywheels that we are studying (i.e., Beacon Power, LLC), are composed of a three component system utilizing: carbon fiber (C-fiber), glass wire (G-wire), and a glue (resin). Figure 2 shows a diagram of the Beacon Power, LLC's Smart Energy 25 Flywheel. This rotor composite is supported by a metal hub and shaft that is attached to the motor/generator. Further to reduce friction, these flywheels are suspended in a vacuum using permanent magnets and electromagnetic bearings. This setup produces flywheels that can reach spin speeds of 16,000 rpm (Mach 2) or higher. These flywheels store rotational energy as kinetic energy, which is proportional to the square of the rotational speed (equation 1). Therefore, when energy is

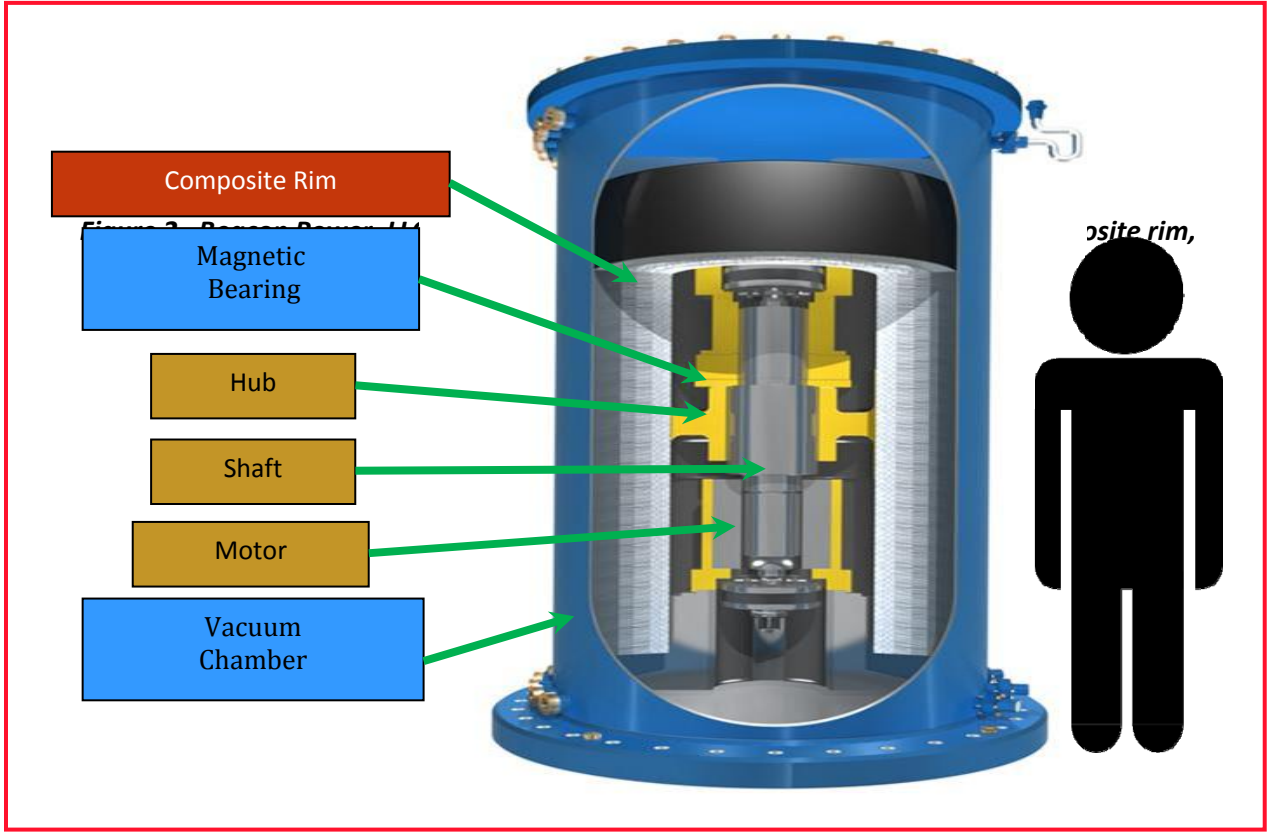

available on the grid, the surplus electricity is used to power the motor, which spins the flywheel at faster speeds, building up kinetic energy. When energy is required by the grid, the motor is switched to a generator mode and the flywheel's accumulated inertial energy drives the generator supplying the grid with the necessary electricity. The flywheels can responds instantaneously and allow for a continuous supply of stable electricity even when the demand and supply fluctuate. A key metric on the performance is determined by the power produced over a period of time – kilowatt-hours (kWh). So, the faster the wheel spins, the more energy that can be stored.

$$E_k = \tfrac{1}{2} I\omega^2 \qquad (1)$$

E_k = kinetic energy, ω = angular velocity, I = moment of inertia

As ‘green’ technologies connect to the AC grid, more energy storage is going to be necessary. This can be handled by simply spinning the flywheels faster; however, the existing composite flywheels are run at near capacity and the faster spin speeds required to handle the ‘green’ energy may result in catastrophic failure. SEM image analysis of the Beacon Power, LLC flywheel component shows the voids and potential break-down sites for a flywheel coupon. Transverse failures are anticipated at higher speeds, possibly originating from the voids observed in the inner and outer part of the ring. Figure 3 shows the TEM images collected.

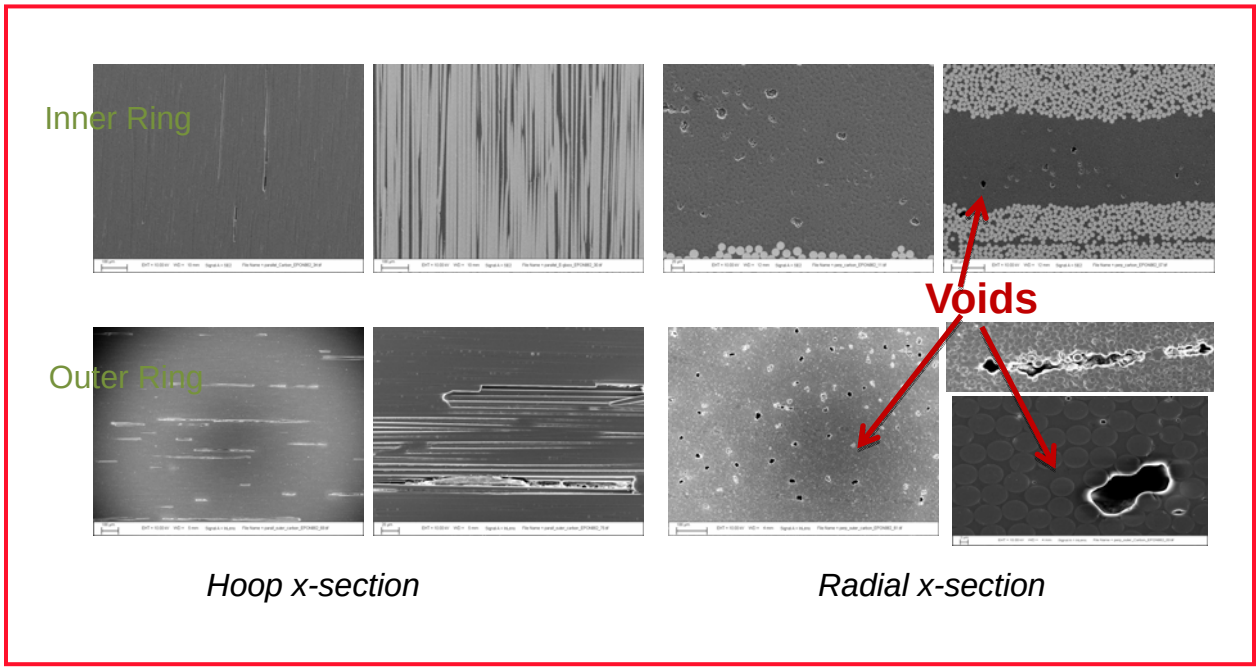

Figure 3. SEM images of Beacon Power, LLC Smart Energy 25 Flywheel Composite rim (a) inner rim and (b) outer rim. Voids are indicated in radial X-section by red arrows.

Therefore, methods to improve the ‘strength’ of the flywheel rim are required (See Figure 4). Of the three components, the resin is the easiest to alter and was the first step explored in this effort. Typically, fillers are added to a matrix to alter the properties. Particle filled composites have found extensive applications in high performance materials ranging from mechanical property tailoring of modulus[1-4] strength, fracture toughness[5] or wear resistance[6] as well as modification of electrical[7] and optical properties[8-10] of the base resin. Epoxy composites with

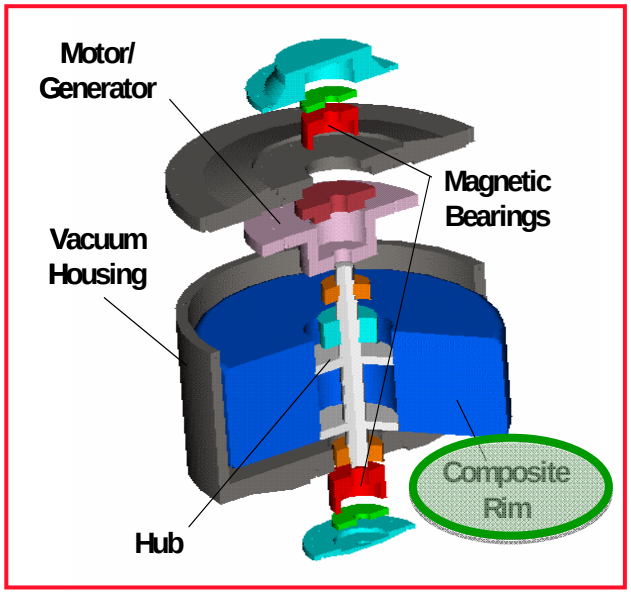

Figure 4. Beacon Power, LLC Smart Energy 25 Flywheel components. Composite rim is highlighted.

particle fillers are also attractive for component manufacture by techniques including injection molding and fiber impregnation, due to the relatively low viscosity of the uncured composition.[11] The preparation of optimum macroscopic properties is related to the content of filler, particle morphology, surface chemistry and reactivity of the filler with the epoxy and also the processing method.[12] Often these fillers must be added at levels approaching 60-70% to impart a significant change in the final matrix properties. This is due to the fact that all the changes occur at the interface of the filler particle and the matrix. Therefore, a standard meso-sized particle only has ~10% of the filler in contact with the matrix, limiting its impact. In contrast, nanomaterials are approaching 90% surface area, which means as a filler, significantly lower levels of material can be added to dramatically alter the properties. Several systems have demonstrated that levels below 5% of nanofillers can significantly alter the properties of the matrix. [12-17] For instance, Guo *et al* found that (3-methacryloxypropyl) trimethoxysilane (MPS) functionalized alumina nanoparticles, when polymerized with a vinyl-ester resin led to nanocomposite that possessed an increased Young's modulus and strength in comparison to the polymer itself.[13] Further, Hong and co-workers found that the glass transition temperatures, surface hardness, flexural strength, impact strength, and tensile properties of polymethyl methacrylate (PMMA) were significantly improved when 7-methacryloxypropyl trimethoxy

silane (KH570) coated nanosilica particles were introduced into the polymer.[14] Significant improvements in the fracture behavior and toughening of nanoplatelet (< 5%) composites were also reported by Boo *et al*.[15] Sarwar details how titania (TiO_2) nanoparticles improved the tensile strength and storage modules of poly(trimethylhexamethyleneterephthalamide) films at maximum improvement between 5 and 10% load levels.[16] From these reports and others,[12,17] uniform mixing and dispersion of nanoparticles in the matrix is critical to achieve consistent macroscopic properties. An understanding of how the particles are stabilized in the uncured system is also important to relate to final composite properties and the operating time for processing.

For this effort, we selected ceramic oxide nanomaterials as the filler for several reasons: (i) large scale preparative routes are available,[18,19] (ii) ceramic materials are easy to functionalize, (iii) relatively inexpensive, and (iv) lend themselves to multiple compositions that will have similar properties. The synthesis of the nanoparticles, their functionalization and characterization were first determined. After this, implementation of these nanomaterials into the resin and its characterization were pursued. Finally, test samples derived from 4" diameter cylindrical samples wound using C-fiber and resin were evaluated using a 'three-point bend' system. The properties derived from these tests and a cost analysis of the improvements noted were determined.

2. EXPERIMENTAL SECTION

The development of the test nanocoupons was undertaken following: (A) Nanomaterials synthesis, (B) Nanowire functionalization, (C) General Nanowire characterization, (D) Dispersion measurements, (E) Surface Charge Measurement, (F) Pellet Pressing, (G) Contact Angle, and (H) Test Specimen. Specifics for each of these processes are discussed fully below.

A. Nanomaterials Synthesis. More specific details concerning the synthesis of nanomaterials used in this effort have been previously disseminated[18,19] but a brief review is supplied below. The following chemicals were obtained from Aldrich and used without purification: TiO_2 nanomaterials (anatase and rutile), KOH, HCl (conc).

(i) nanowires: A TiO_2 sample (7.50 g, 9.38 mmol) was suspended in 10 M (aq) KOH (~500 mL volume held constant) in a 1 L Nalgene™ (polymethylpentene) bottle and heated for 3 d at 125 ^oC inside an oven with the cap loosely screwed on to prevent pressure build up. Additional water was added every 12 h to maintain the original volume level. After heating for 3 d, the reaction was allowed to cool to room temperature and the resulting powder isolated by reducing the pH to below 7 and then adding acid to achieve neutrality. Larger amounts were prepared by running several reactions side by side in the oven. The nanowires formed were identified as the $H_2Ti_2O_5 \bullet H_2O$ structure.

(ii) Nanosquares: Rutile TiO_2 (0.200 g, 2.50 mmol) nanoseeds were added to 10 mL of DI H_2O in a Teflon™ sleeve of a Parr™ digestion bomb, followed by 10 mL of the desired conc. HX (X = Cl, Br, I). The reaction was sealed and then heated at 225 ^oC for 24 h. After this time, the reaction was allowed to cool to room temperature, the precipitate separated from the mother liquor by centrifugation, and washed three times with DI water. The resulting powder was dried thoroughly in an oven at 130 ^oC).

B. Nanowire functionalization. For the HYBR produced TiO_2 nanowires that were further modified, a solution of either (i) silane/EtOH/H_2O [5/5/90 (v/v/v)] or (ii) silane/solv [solv = THF, toluene, or toluene/py (5/95 (v/v)] using 3-aminopropyl trimethyl silane (ATS), triethoxy silane (TEOS), or dodecyltriethoxy silane (DTS) was prepared. To each of these solutions, TiO_2 (0.300 g) was added and heated at 35^{o}C for 4-12 h. The reaction mixture was then sonicated for 1 h. The products were dried in an oven (130^{o}C for 1 h) and then used for ζ-potential measurements.

C. General Nanowire Characterization. A Varian 2000 FT-IR (Scimitar Series) spectrometer was used over the range of 400-4000 $cm^{-1}$to analyze the TiO_2 nanomaterials. Transmission electron microscopy was used for morphology characterization of each TiO_2 powder with either a Philips CM 30 TEM or a FEI Tecnai TF30 TEM/STEM, operating at 300 kV accelerating voltage. A TriStar 3000 BET instrument from Micromeritics Instrument Corporation 4356 Communications Drive Norcross, GA 30093-2901 was used to measure the surface area of the five types of TiO_2 nanopowders.

D. Dispersion Measurements. Powders were dried under vacuum at 90 °C overnight in order to remove surface adsorbed water. Small contents (~100 mg) were added to the anhydride component of epoxy compositions. The three chemicals used include methyl nadic anhydride (Sigma-Aldrich, MNA), hexahydro-4-methylphthalic anhydride (Sigma-Aldrich, HHMPA), and commercial ECA100NA component (65% HHMPA, 10% MNA, 25% Dixie Chemical Co. Pasadena, TX, 77507). These dispersions were formed by ultrasonic mixing using an ultrasonic

probe (Branson Ultrasonics, 250 W) at 60% power in an ice bath, and an ultrasonic cup horn with water bath set to 50 °C (Branson Ultrasonics, 450 W) at 90% power. The materials were sonicated for 20 minute sessions in 0.5 sec pulsed modes in either ultrasonic device until no sediment from the original material was evident. This process required several cycles (over 5 in each case). The dispersions were then immediately diluted to transparency for measurement of particle size in a light scattering instrument (Malvern Zetasizer NS from Malvern Instruments Ltd, Enigma Business Park, Grovewood Road, Malvern, Worcestershire WR14 1XZ, United Kingdom). Ten measurements of the particle size distribution for each sample were conducted, and averaged to estimate the degree of dispersion of each system.

E. Surface Charge Measurement. Zeta potential (ζ–potential) measurements were conducted using a Malvern Zetasizer NS instrument for the initial powders as a function of pH (using HNO_3 and KOH for adjustment) in 10^{-3} M KNO_3, and for the dispersed particles in each anhydride fluid, and after collection using an ultracentrifuge and ultrasonic re-dispersion in both tetrahydrofuran (THF) and water solvents. The centrifugation method was also used to collect the anhydride dispersed particles from each liquid and washed clean using five cycles of centrifugation and redispersion in THF. The dried particles were tested for surface modification using a Varian 2000 Scimitar Series FT-IR, and tested over the range of 400-4000 inverse wavenumber.

F. Pellet Pressing. Pellets were pressed without using binders from each powder sample. A 0.25” die was used for pellet production with approximately 0.5 g of powder. Teflon™ pipe tape was used over the flat ends of the die press to prevent material contamination and to allow for

removal of smooth pellets from the die. Applied pressure of 8,000 to 13,000 lbs was used to compact each pellet. The removed pellets were then sealed in elastic bags and iso-pressed at 30 ksi. Pellets could only be pressed and iso-pressed for the Aldrich anatase powder, and the two wire morphologies. The rutile rods would not survive the iso-pressing state, and in the pellets that were made, the porosity of the pellets lead to rapid adsorption of the probe liquid, leading to failure to get good values.

G. Contact Angle. Contact angle measurements were conducted on smooth faces of the pellets using a Kruss DSA 1 Instrument, with 1-bromonaphthalene, di-iodomethane, glycerol, water, formamide and tetrahydrofuran solvents. Pellets were dried between measurements under vacuum to remove residual solvents. At least three measurements of advancing contact angle were used in each system to evaluate the wetting interaction. A Teflon™ film was also polished to optical smoothness and used to evaluate the wetting of each anhydride liquid as well as the probe liquids.

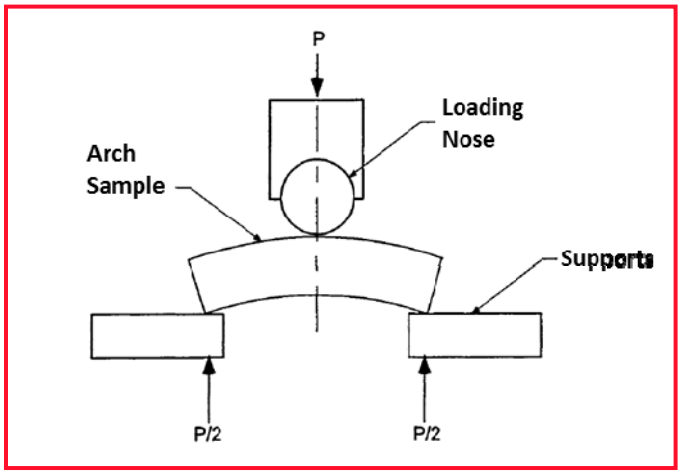

Figure 5. Diagram of 3-point-bend test geometry for the measurement of the interlaminar shear strength of composite arch samples.

H. Test Specimen. Filament wound carbon fiber composite tubes were fabricated from the neat resin systems and resin systems with dispersed nanomaterial. The carbon fiber was TorayCa T700S. The composite tubes had dimensions of 4 inches I.D., 0.25 inch thick wall, and 12 inches long. The winding parameters were as follows: 22 rpm wind speed, 6-6.5 lbs line tension at the part, single

tow, hoop wound. The composite tubes were cured according to the recommended cure procedure to obtain complete cure. The tubes were rotated at 5 rpm to prevent flow of the resin during cure. Composite tubes were cut to obtain arch samples with arch length of 1 inch, width of 0.5 inch, and thickness of 0.25 inch. The composite arch samples were tested by 3-point-bend according to ASTM D2344 to failure. Figure 5 shows a diagram of the sample test geometry. The inter-laminar shear strength was calculated from the maximum load at failure through equation 2.

$$\tau_y = 0.75\,[P_{max}/(b \times h)] \qquad (2)$$

τ_y = interlaminar shear strength, P_{max} = maximum applied load at failure, b = width of the arch, h = thickness.

3. RESULTS AND DISCUSSION

In order to generate the highest impact at lowest load level of the TiO_2 nanofiller, it is critical that they be uniformly distributed throughout the matrix of interest. [12-17] There are several processing steps that must be followed to achieve control over the homogeneity of a particle reinforced composite. The removal of adsorbed water on the TiO_2 surface minimized solvophobic aggregation and poor dispersion, surface modification to improve bond strength between the nanofiller and the epoxy matrix, and ultrasonic or other high energy mixing processes are all important.[20,21] Typically, epoxy nanocomposites require pre-mixing the filler in one of the two reactive components first (epoxy or hardener agent), to develop a homogeneous dispersion, and then combining that mixture with the second reactive component. A volatile co-solvent can be used to lower the viscosity of the system during this process, which is accomplished with high shear mixers or ultrasonic dispersion.

For effective dispersion of the TiO_2 nanofillers, a processing strategy that overcomes the Van der Waals attractive forces between any homogenous particle system, a stabilization mechanism of the particle in the matrix is necessary, and a method to overcome the surface wetting issues (i.e., hydroxyl groups) of the TiO_2 nanomaterials. Often this is realized by functionalizing the ceramic materials with an organic group that has a strong mixing interaction with the matrix (or initial component). Silane surface modification of ceramic materials has been successfully realized such that several industrial relevant applications utilize this process.[22] Often the effectiveness of the dispersion is inferred from mechanical properties in the solid final component or by examination of a fractured surface using spectroscopic methods. Characterization of the state of aggregation can easily be conducted in the unreacted fluid state using light scattering techniques, which relates to the initial state of the particle stability and effectiveness of particle dispersion.

In epoxy systems, it is more common to surface modify the filer with an amine bearing chemistry, to promote covalent bonding between the reactive epoxy network and the inorganic surfaces, including aminopropylsilane and tetraethoxytriamine (TETA). These molecules will create a short steric interaction, which may not prove sufficient to stabilize all the particles. During the crosslinking or curing reaction, polymer material is formed with increasing growth in the effective radius of gyration. In the event that the polymer system can gain entropy by being excluded from the interparticle gap, depletion forces can be generated that will cause agglomeration between the particles despite the steric separation between the surface modifying groups. A process leading to a thin surface layer around each particle containing reactive groups is a good potential route to obtaining a well-dispersed system of metal oxide in an epoxy formulation.

The following discussion focuses on the development of improved flywheel materials through the introduction of a variety of functionalized TiO_2 materials of different shapes to determine optimal dispersion. The resin used for this study was determined to be EPON862, which was based on a previous effort to identify a resin that would yield the strongest interaction. This was done by generating both a glass and carbon tube, which was subsequently segmented and tested by a three point bend method. From these results the EPON862 (Figure 6) had the highest strength for both the carbon and glass fiber. The C-Resin interaction was found to be the weakest by microdroplet test (Figure 7a-c). This was further verified by SEM analyses, which showed a clean C-fiber versus the glass after exposure to the resin (Figure 8a-b). It is of noted that a 50 ^{o}C increase in the processing temperature leads to a more than 5 times increase in the fiber resin interaction (Figure 7d-e); however, the program demanded that minimal processing changes be incurred. All additional studies focused on C-fiber and resin interactions.

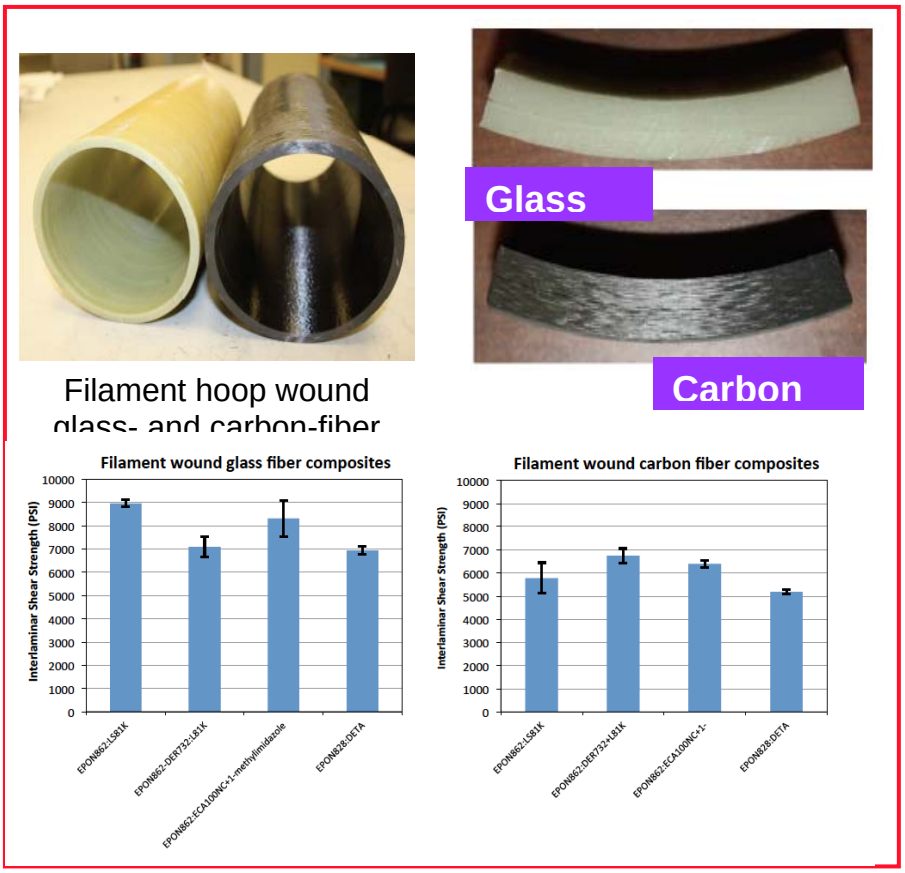

Figure 6. Top pictures are of sample winding tubes. Graphs represent intrinsic shear strength of the samples as determined by 3-point bend test using (a) EPON862, (b) an epoxy anhydride, (c) an epoxy anhydride + catalyst, and (d) epoxy amine.

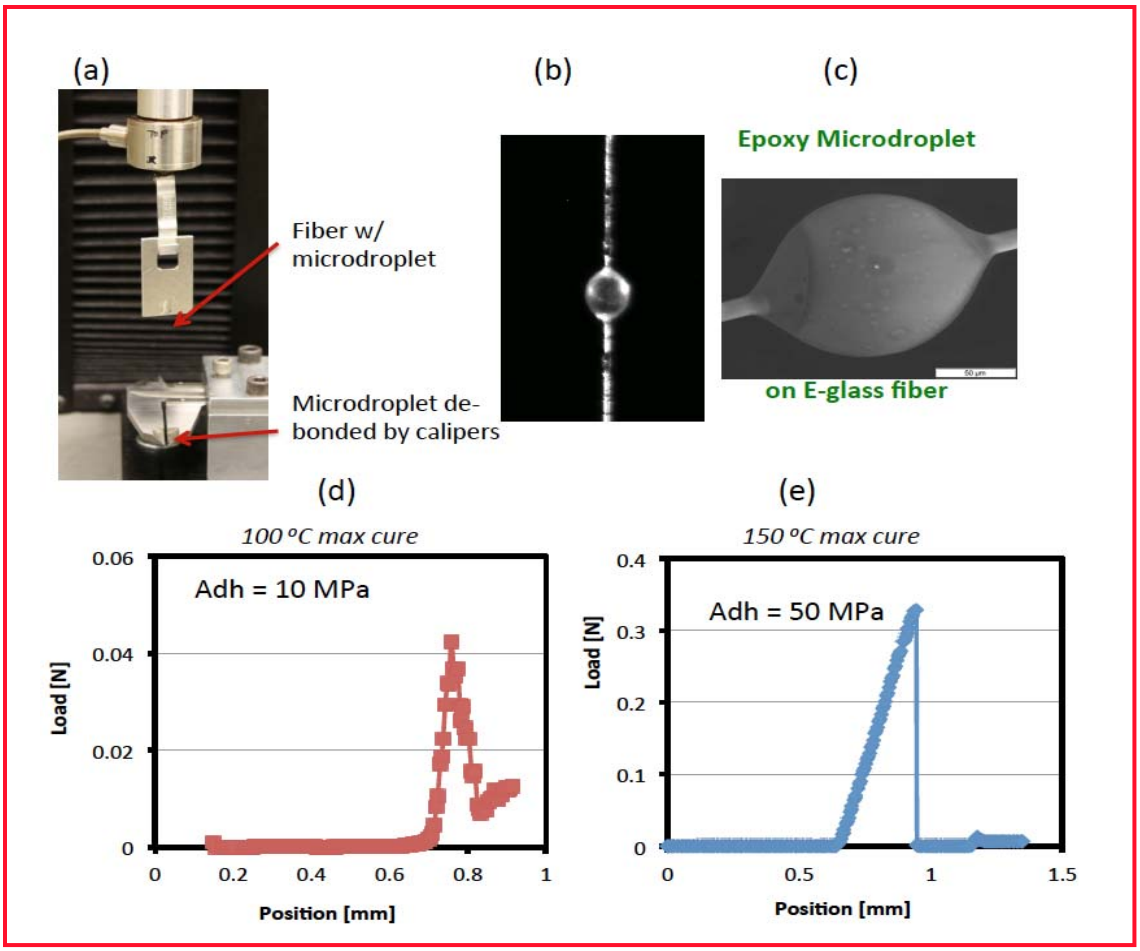

Figure 7. Microdroplet test showing test methodology 9a) setup, (b) sample on glass fiber, (c) enlarged image, (d) sample heated to 100 ^{o}C, and (e) sample

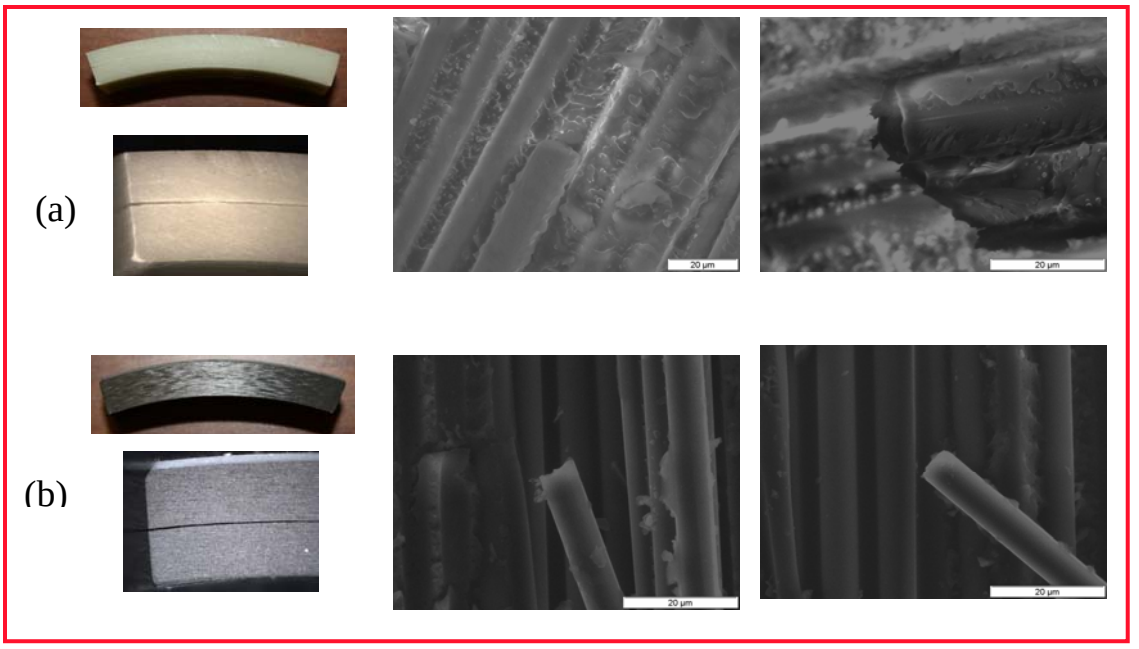

Figure 8. Image sof 3-point bend damaged samples (a) glass and (b) carbon fiber. Left images are picture of the arc sample (top), broken sample (bottom). Right SEM images of the broken fiber.

Using EPON862, a set of different functionalized TiO_2 nanowires were added with mixing. These were then wound to generate test specimens, which were evaluated for variations in their final properties. These are discussed in detail below. We have focused on (A) *nanomaterial synthesis* of large scale, functionalized TiO_2 nanowires, (B) *Functionalization* of the TiO_2, (C) *Nanomaterial Characterization*, (D) *Nanomaterial dispersion in anhydride*, (E) *Nanomaterial dispersion in epoxy*, (F) *Nanomaterial nanofiller selection*, and (G) *Composite test sample analysis*. Once finalized, the economic impact that the changes wrought from the introduction of nanowires were estimated (see Section 4). These are presented in order below.

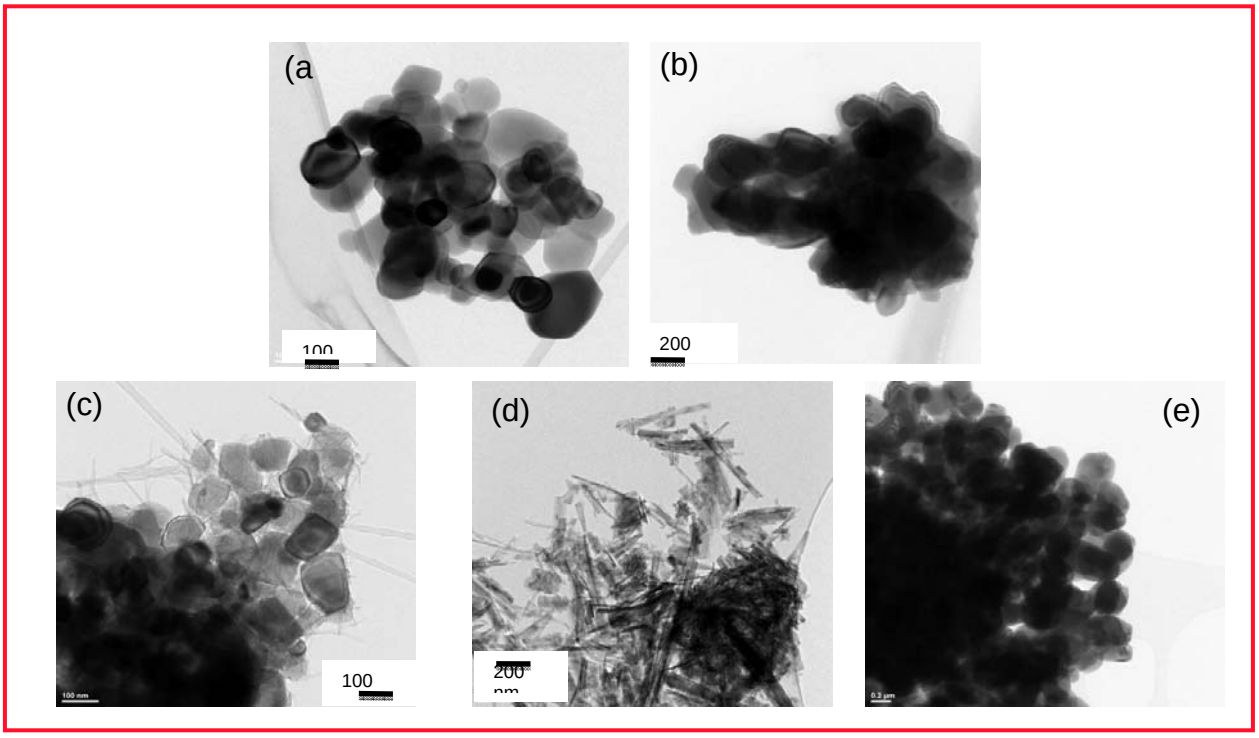

Figure 9. TEM images of morphology of titania nanoparticles: (a) Anatase nanodots (Aldrich) (b) Rutile nanorods (Aldrich) (c) nanowires formed by the HYBR route; (d) nanorods formed by the SOLVO route (e) faceted nanoparticles acid HYBR route.

(A) *nanomaterial synthesis*. The initial synthetic efforts focused on generating the large-scale (~500 g per test sample/ 3 sample sets) amount of TiO_2 materials necessary to evaluate the

different resin systems of interest. Several processing routes were evaluated with the HYBR route[18,19] finding favor, since multiple reactions could be run simultaneously with a relatively inexpensive (plastic bottle) setup. Further, the variety of nanoparticle morphologies available based on the solvent (acidic, basic, neutral) [18,19] was also attractive since it would allow for the evaluation of morphological impact, which has been reported to be a significant factor, [12,17] on the final strength of the flywheel test specimen as well. The synthesized and commercial nanomaterials initially evaluated are shown in Figure 9.

After the appropriate evaluation (*vide supra*), it was decided that the nanowires would be the most impactful based on the high aspect ratio of the TiO_2. From five to six 'batches', we successfully produced more than 500 g of TEM characterized TiO_2 nanowires. The synthesis involved the mixing of the nanodots of anatase (Aldrich – Figure 9a) in 10 M KOH and heating at 125 ^{o}C for 3 days. Afterwards, the solution was neutralized with HCl and the nanowires separated by centrifugation. One representative TEM image from these different reactions is shown in Figure 10. Each reaction mixture was checked and verified to be of similar morphology before combining with in-hands samples of TiO_2 nanowires. These so called 'naked' nanowires were then used as the source for functionalized nanomaterials that would be used as the filler in the test specimens.

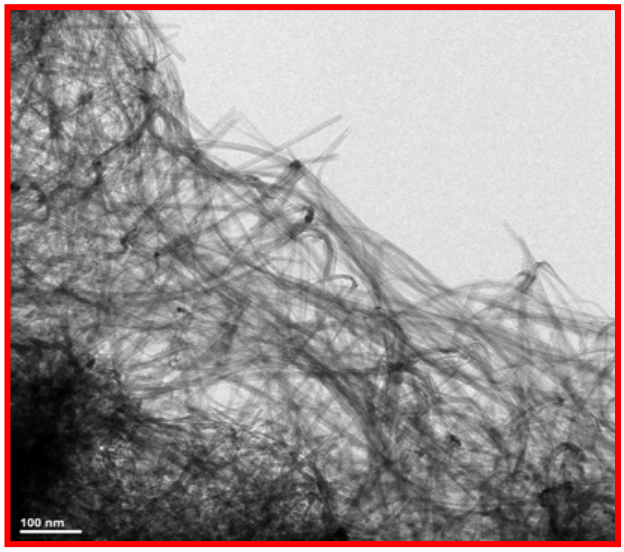

Figure 10. Representative TEM images of TiO2 nanowires synthesized by the HYBR route.

(B) *Functionalization*. With the TiO_2-NW in hand, the next step was to functionalize them with identical 'anchors' (sites that bind to the nanoparticle) but varied in the terminal functional group (i.e., alkyl, amine, thiol, etc). The silanes were selected based on their previous utility in functionalizing other ceramic materials[23,24] and the commercial availability of different variants. The naked TiO_2-NW were slurried in a solvent ($MeOH/H_2O$, toluene, toluene/py, or THF) with the silane (i.e., 3-aminopropyl trimethyl silane (ATS), triethoxy silane (TEOS), or dodecyltriethoxy silane (DTS)) added. The reaction was heated and dried to allow for fully formed silica shell coating. Some TEM images of the products were collected and are shown in Figure 11 to determine if any impact was observed on the morphology. The rods shown do not appear to be altered by all of the modifications undertaken. Therefore, it was important to characterize the properties of these materials.

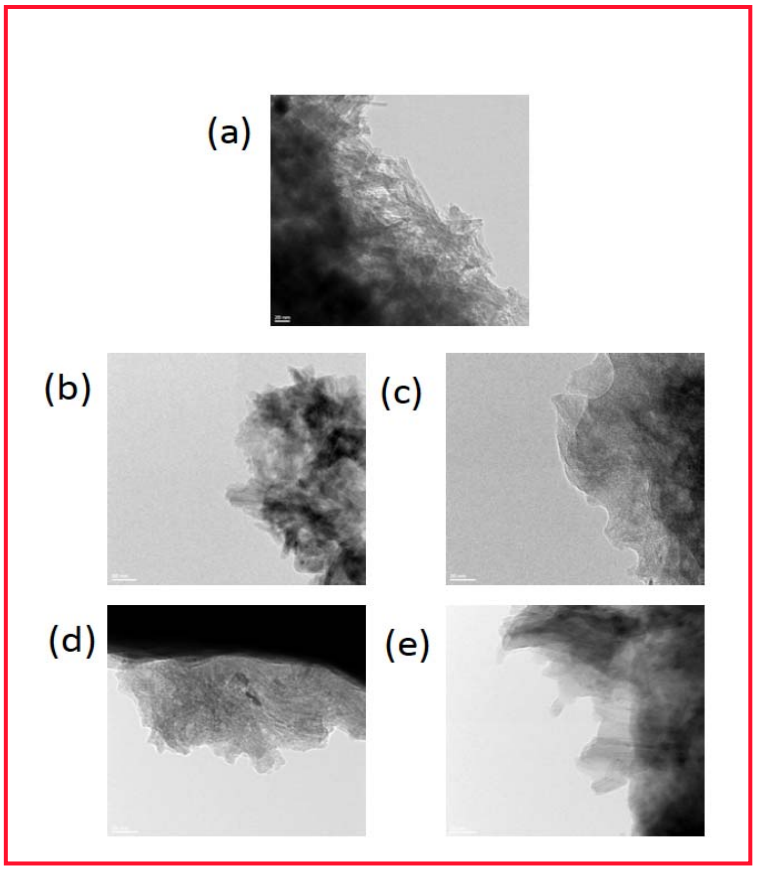

Figure 11. TEM images of (a) naked TiO_2 rods, functionalized with SiO_2 from TEOS in (b) $MeOH/H_2O$, (c) toluene, (d) toluene/pyridine and with (e) aminosilane from ATS in $MeOH/H_2O$ (heated to 180°C to remove solvent).

(C) *Nanomaterial Characterization.* The surface properties of the different shaped 'naked' TiO_2-nanomaterials (Figure 10) were first evaluated in context of the epoxy hardener materials

as well as the dispersion in the anhydride component. Van Oss theory for wetting interactions is applied to understand the driving force for wetting of the particles in relation to the effectiveness of the processed nanoparticle dispersion. Surface modification by reaction of the anhydride component with the TiO_2-NW surface was investigated to establish if reaction leads to stabilization. Attempts were made to measure ζ-potential (zeta potential measures the charge on the surface of a materials, Figure 9) under similar conditions to that of the processing scheme in order to determine if an electrostatic stabilization mechanism was operating between the TiO_2-NWs. Table 1 presents the results for this characterization.

Table 1. BET Data for TiO_2 nanopowders

Sample	Surface Area (m^2/g)	Langmuir Surface Area (m^2/g)
TiO_2 (Nanotek)	40.98 ± 0.09	57.18 ± 1.34
Anatase (Aldrich)	82.62 ± 0.30	114.40 ± 2.95
Rutile (Aldrich)	3.60 ± 0.01	5.05 ± 0.13
Hybrid TiO_2-NW	130.16 ± 0.53	180.37 ± 4.79
Rods (Anatase , Rutile)	190.32 ± 0.57	263.29 ± 6.48

The ζ-potential vs. pH curves shown in Figure 12, serve to characterize the acid-base character of the various nanopowders. Reactivity of the surface to the epoxy or anhydride phase can be influenced by the surface chemistry of the filler particle. The presence of residual hydroxyl groups on the powder surface will prevent dispersion of the powder in the epoxy phase due to poor wetting and hydrogen bonding of the surface. Thus, the reaction of the surface hydroxyl

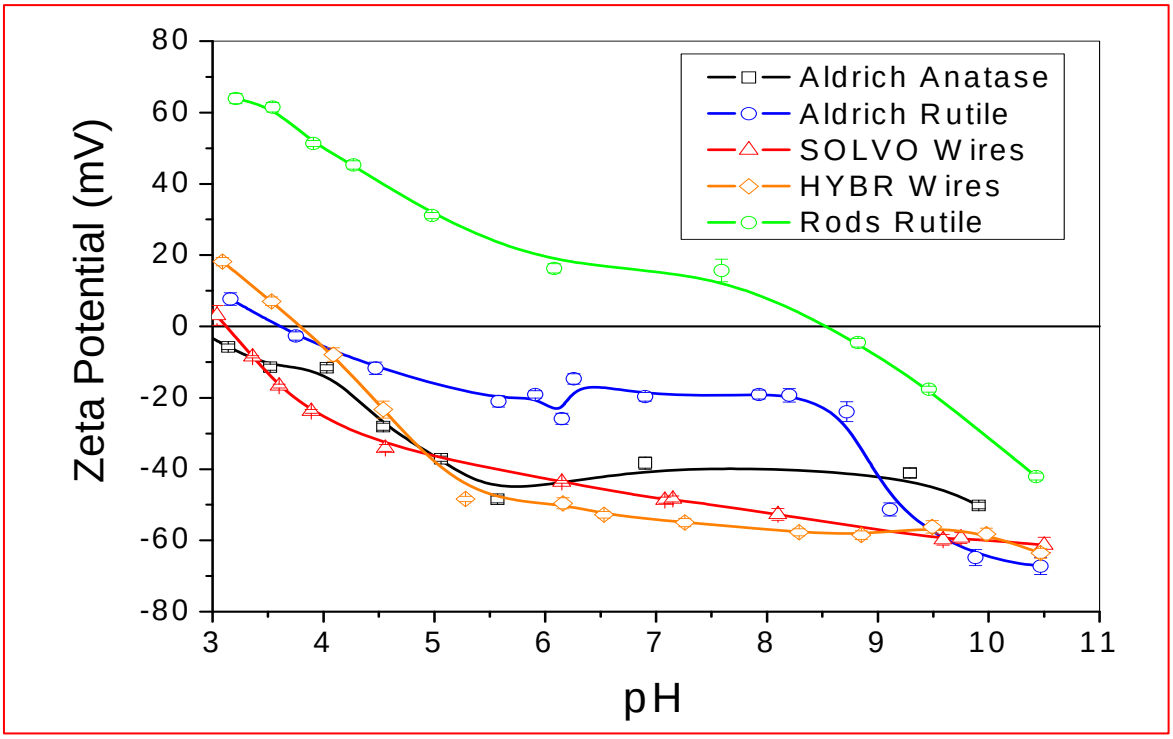

Figure 12. ζ Potential of initial titania nanoparticles vs. pH. Background electrolyte is 10^{-3} M KNO_3 aqueous solution.

groups to allow wetting is of primary concern for successful dispersion of a filler particle in epoxy. The ζ-potential is derived from the protonation or deprotonation of the terminal surface groups for each nanopowder and is effected by surface facets through the coordination of surface metal cations with local oxygen ions in the crystal structure, the number of adsorbed hydroxyl groups, or the specific adsorption of counter ions. The development of charged surface groups (positive and negative) occurs in relation to the acid and base properties of the solvent and its capacity for protonation. The point at which a suspended particle exhibits no response to the applied field infers that the number of positive and negative surface groups are equal (i.e., neutral).

The majority of the TiO_2 nanopowders have a low isoelectric point (IEP) between 3-4. The surface groups of these samples are generally expected to be terminated with –OH groups, so these groups are very likely to donate a proton to a water molecule and become a negatively

charged surface group $-O^-$. Both wire morphologies have a smooth type of curve, whereas the Aldrich Anatase and Aldrich rutile phases seem to plateau in the 5-8 pH range before increasing again at higher pH values. This could mean that there is more than one type of surface group and varying pK_a values. The Aldrich rutile powders have lower magnitude of ζ–potential in the mid range pH region, so the number of reactive groups may be lower than the Aldrich anatase powder. The smoother profiles of the wire morphologies can reflect dominance of the wire sidewall chemistry on the surface charging, where the electrostatic charging of neighbor groups broadens the protonation behavior similarly to the charging electrostatic effects in polyelectrolytes. The rutile rods are the only material that shows a high value for the IEP of about 8.6. Its behavior is typical for hydroxyl surface groups, and the value of the IEP is still within the range expected for TiO_2. This sample was formed by the acid process, and therefore appears to have stabilized with surface facets having a positive surface charge over much of the surface.

To characterize the surface chemistry of each powder after exposure to the anhydride hardening agent of the epoxy, the powders were collected by centrifugation and washing with dimethylformamide. After five cycles of centrifugation and dispersion, the particles were allowed to dry at 90 °C overnight. The dried particles were tested for surface modification using IR spectroscopy. Use of these materials in the anhydride solvent during the first stage of epoxy composite preparation has been noted to result in the rapid reaction of the anhydride to the TiO_2 surface.[25] The surface reaction of each nanopowder with the anhydrides was characterized using FTIR, and is presented in Figure 13. All the nanopowders initially have a broad peak ranging

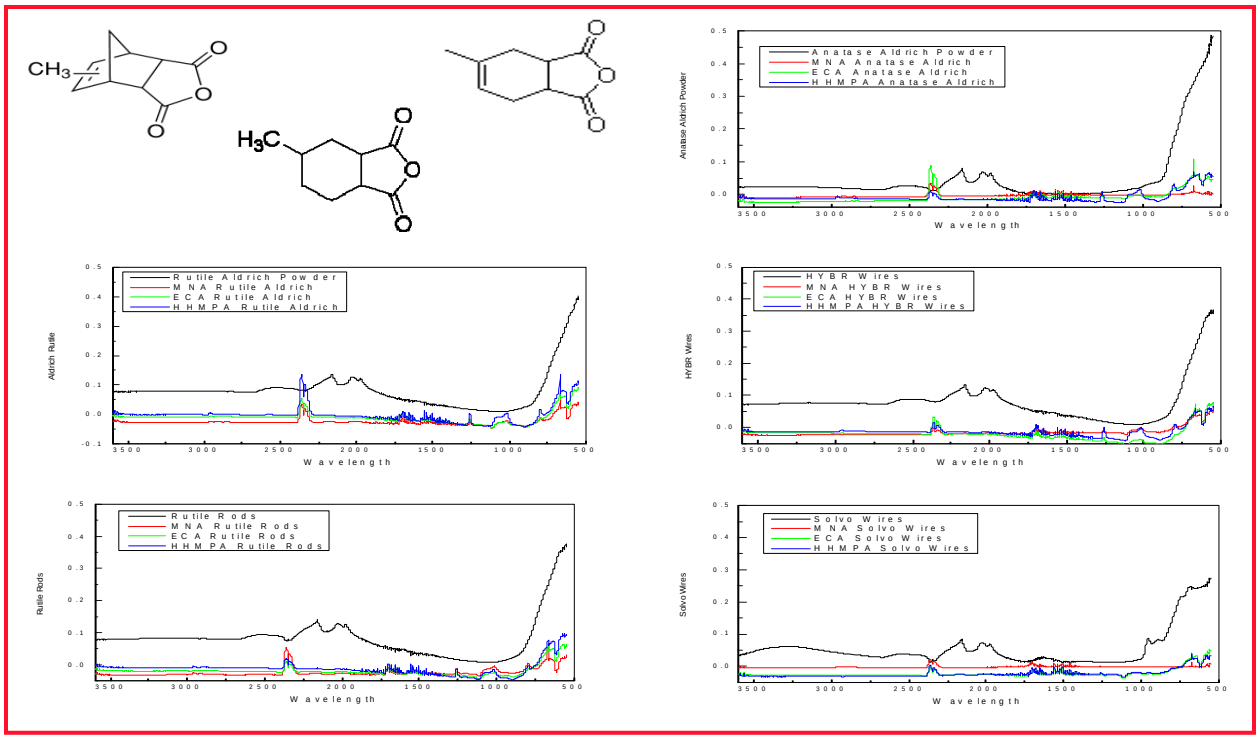

Figure 13. Surface reaction characterization of TiO_2 nanoparticles with anhydride hardeners used in epoxy composites.

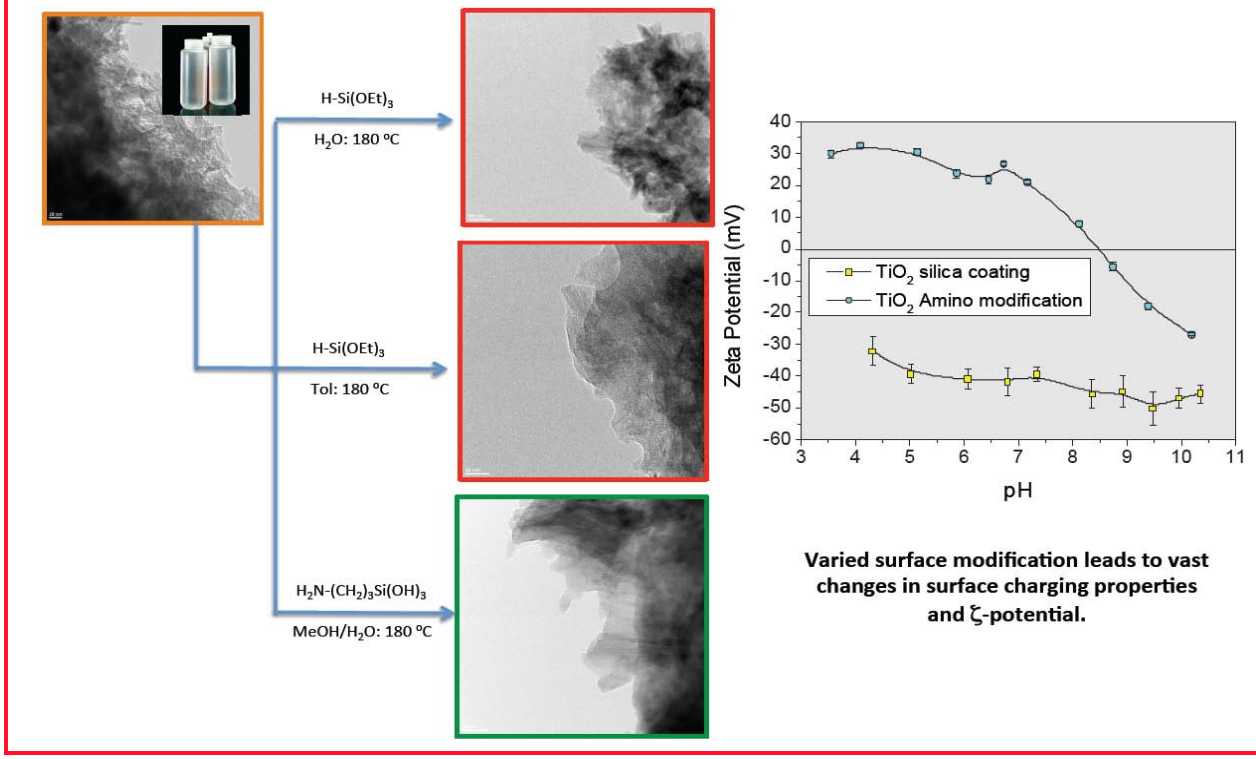

Figure 14. TEM images of silane functionalized TiO_2-NW and the subsequent ζ-potential measurements.

from 3600 to 2800 cm^{-1}, ~2800 to 2400 cm^{-1}, and sharp peaks near 2200, 2000 cm^{-1}, and 1800 cm^{-1}. After exposure to the three anhydrides studied in this system, the intensity of these characteristic peaks is greatly diminished, and more evident peaks from surface reaction are noticeable at 2360, 2340 cm^{-1}, and 1240-1260 cm^{-1}. Broader peaks are located at 1075-1086, 1018, and 795 cm^{-1}. These FTIR spectra do not support the literature assertion that the anhydride adsorbs to form a carboxylate termination. There are changes from the neat powders, including the removal of the –OH vibration in the range 3600-2300, by the solvent exposure. This suggests removal of the adsorbed water and the surface hydroxyl groups. However, the normal peaks associated with anhydrides are located near 1825 cm^{-1}, and with carboxylic acids in the range of 1750-1776 cm^{-1} are missing. Perhaps the anhydrides are adsorbed through the three oxygen atoms without bond breaking, leading to the shifting of peak locations.

Using the HYBR generated materials (Figure 10), the samples were modified by a variety of silanes under different conditions. Figure 14 shows the TEM images of the materials and the ζ-potential measurements for the final materials. As can be observed, the ζ-potential indicates that the surfaces have been altered. The TEM indicates that some changes may have occurred on the samples but for the silane/H_2O system, wires are retained.

(D) *Nanomaterial dispersion in anhydride.* After removing the surface absorbed water by vacuum drying (90 ^{o}C), each of the TiO_2 samples were characterized for dispersion in the anhydride. Small contents (~100 mg) were added to the anhydride component of epoxy compositions including, methyl nadic anhydride (MNA), hexahydro-4-methylphthalic anhydride (HHMPA), and commercial ECA100NA epoxy curing agent. The dispersions were then immediately diluted to transparency for measurement of particle size in a light scattering

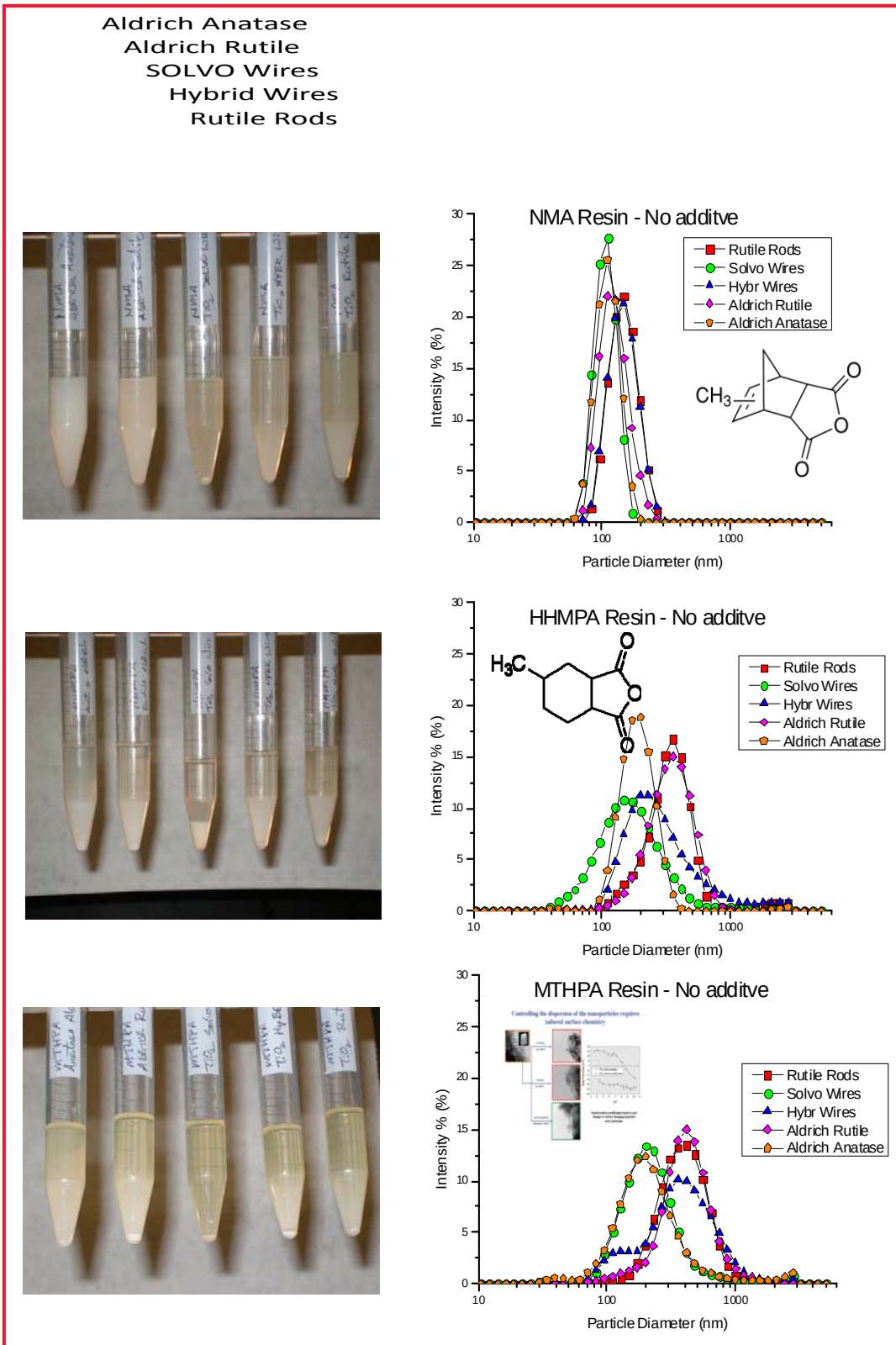

Figure 15. Dispersion Characterization of TIO_2 nanopowder in each anhydride hardener. Sedimentation images for each powder are shown on the left for one week settling. The graphs on the right show the particle size distribution after sonication. NMA solvent supports dispersion to ~100 nm particle size, which does not sediment. The other solvents led to sedimentation of larger particle materials.

instrument (Malvern Instruments Zetasizer NS). Figure 15 shows the image of the suspension of each system and the particle size distribution of each powder measured by light scattering. Of all the solvents, the methyl nadic anhydride provides the smallest particle size. These powders in MNA also show dispersed powders after allowing for particle settling. The other two resins show systems in which the particles have sedimented out of the dispersion. The MNA solvent has the highest viscosity of all three anhydride liquids, whereas other properties of the fluids such as density or dipole moment are very similar. The molecular structure of MNA is more sterically bulky due to the tertiary carbon bonds in the ring structure in contrast to HHMPA and the ECA100 fluids. Further study is needed to determine if any factor other than the higher viscosity of the MNA solvent might lead to particle dispersion or stability. Without another mechanism, the particles in MNA would be considered only kinetically stable, and could precipitate during the cure reaction at elevated temperature.

Several routes to different shaped nanoparticles were initially investigated to determine which would be appropriate for inclusion into the resin. An attempt to measure the surface wetting characteristics for each powder was made using contact angle measurements. Discussion of the measurements and results follows in the next section.

(E) *Nanomaterial dispersion in epoxy.* Van Oss Theory (calculations concerning the surface energy and wetting properties of nanoparticles) is commonly used for relating dispersion to nanocomposite performance. Wetting measurements taken from contact angle studies are used to determine the surface parameters of solids, leading to total surface energy, and the detailed breakdown of the surface components into Van der Waals and polar (acid and base) components

of surface energy. The expression for the interaction between the components of the surface energies of the liquid and solid phases is as follows in equation 3:

$$\gamma_{SL} = \left(\sqrt{\gamma_S^{LW}} - \sqrt{\gamma_L^{LW}}\right)^2 + 2\left(\sqrt{\gamma_S^+\gamma_S^-} + \sqrt{\gamma_L^+\gamma_L^-} - \sqrt{\gamma_S^+\gamma_L^-} - \sqrt{\gamma_S^-\gamma_L^+}\right) \quad \textbf{(3)}$$

It is necessary to make contact angle measurements using three different liquids, all with known values of γ_L, γ_L^{LW}, γ_L^+ and γ_L^-. Then, solving three equations in three unknowns provides the values of γ_S^{LW}, γ_S^+ and γ_S^-, which can then be used with equation 4 to determine γ_S:

$$\gamma_S = \gamma_S^{LW} + 2\sqrt{\gamma_S^+\gamma_S^-} \quad \textbf{(4)}$$

The obtained values of γ_S can then be used with the known values of γ_L in equation 5 to determine γ_{SL}.[1]

$$\gamma_L \cos\theta = \gamma_S - \gamma_{SL} \quad \textbf{(5)}$$

A high dispersion of particles is achieved in epoxy systems by improving wetting interactions with the filler particles, using either surfactants, surface modification or a co-solvent. Epoxy nanocomposite reviews state that “good” wetting requires the matrix to have lower surface energy than the reinforcement phase, so that an epoxy with a surface tension of 39 mJ/m^2 will wet glass or carbon fibers of surface energy ranging from 40-60 mJ/m^2.[16,25]

Pellets of the TiO_2 nanomaterials were generated as described in the experimental section. Contact angle measurements were conducted on smooth faces of the pellets using a Kruss DSA 1 Instrument, with 1-bromonaphthalene, diiodomethane, glycerol, water, formamide and tetrahydrofuran solvents. The results from this study are listed in Table 2. Pellets were dried between measurements under vacuum to remove residual solvents. At least three measurements of advancing contact angle were used in each system to evaluate the wetting interaction. Pellets could only be pressed and iso-pressed for the Aldrich anatase powder, and the two wire

morphologies. The rutile rods would not survive the iso-pressing state, and in the pellets that were made, the porosity of the pellets lead to rapid adsorption of the probe liquid, leading to failure to get good values.

Table 2. Contact angle for liquids over pressed pellet samples.

	Aldrich Anatase	**HYBR Wires**	**SOLVO Wires**
Bromonaphthalene	21.8 ± 9.23	9.92 ± 6.74	41.86 ± 8.91
Diiodomethane	6.67 ± 5.7	32.2 ± 9.16	51.42 ± 9.82
Formamide	10.93 ± 4.85	42.3 ± 5.58	55.83 ± 7.82
Glycerol	39.8 ± 9.04	73.8 ± 4.72	83.4 ± 2.89
Water	12.08 ± 5.93	62.7 ± 13.76	79.34 ± 2.74

Wetting parameters for the surfaces are determined by solving the wetting equation (6). The values are presented in Table 3. The solution was made using the contact angle values measured for diiodomethane, glycerol and water. These materials have the highest surface tension values, and should have provided the highest contact angles to give more accurate results. From Tables 2 and 3, it is not clear if the pellet wetting technique was successful in determining true surface property values. Porosity in the pellet can lead to an abnormally low value for the contact angle, which would be reflected in the viscosity of the fluid. For example, the contact angle for water in the Aldrich anatase pellets is very low, whereas the value is much higher for the HYBR and SOLVO samples. Conversely, the HYBR wires have a very low value for bromonaphthalene,

$$(1+\cos\theta)\gamma_L = 2(\sqrt{\gamma_S^{LW}\gamma_L^{LW}} + \sqrt{\gamma_S^{+}\gamma_L^{-}} + \sqrt{\gamma_S^{-}\gamma_L^{+}}) \qquad \textbf{(6)}$$

Table 3. Calculated Surface Wetting Parameters for TiO_2 particles.

	γ^{LW}	γ^+	γ^-
Aldrich Anatase	48.93	59.63	0.004
HYBR Wires	42.27	30.88	1.11
SOLVO Wires	32.83	15.89	0.55

yet the anatase sample has a low value for diiodomethane. Overall, the anatase samples have lower contact angles for every fluid. When these parameters are used for determining the contact angle results, it provides a higher value for the dispersive, Lifshitz-van der Waals term (LW), which one would expect to be fairly constant due to the relatively similar nature of the titanium oxide. Also, the Lewis acid term (electron acceptor) term for each material is very high. The zeta potential values characterized in water show that the surface property is acidic, and therefore is expected for these materials. As they all have a very low isoelectric point, the near negligible term for Lewis base properties is also valid. However the magnitude of these terms is questionable, as the value for anatase exceeds a realistic value for the surface tension of the powder.

Determination of the wetting parameter of the epoxy fluid is needed to determine the wetting interaction energy ΔG_{131} for dispersion of these powders, and is to be completed in future work. Wetting measurements for these materials will also be compared to wetting over a film and evaluation by the Washburn equation in future work.

(F) *Nanomaterial nanofiller selection.* Based on the above analyses, it was decided that the TiO_2 nanofillers would be an adequate model system to investigate the modification to the EPON resin. Of the different shapes, the nanowires were selected due to their distribution in the anhydride resin system. Further, it was clear that the silane functionalized nanomaterials would assist in the distribution of the nanofillers. Three samples were selected to be investigated (a) naked, (b) APTMS (Amino propyltrimethoxysilane), and (c) MPCA. A 5% loading of TiO_2-NW was chosen as a compromise between a high loading and low viscosity impact necessary to not impinge on the processing effort. A high loading is desired to impart the greatest amount of added strength to the resin, but high loading increases the viscosity of the resin making fabrication of composite structures more difficult. A 5% loading allowed a viscosity that was still conducive to filament winding.

For each of the samples, 500 g of nanowires were generated, functionalized and added to the EPON 862 part of the resin system. These were then supplied to the Air Force Research Laboratory along with the carbon fiber (T700S 12K 50 C) or glass fiber (PPG Fiber Glass – 1063 Roving) to be wound onto a 1.5 inch mandrel that was wound as close to 0^o as possible at a 22 rpm speed. The spools of fiber go through a 3 part resin bed (EPON 862, LS-81K, and BYK A-525) prior to being wound. The wires were held at zero degrees to impart the highest hoop stress, give the hoop direction the highest modulus (limited amount of growth in the radial direction), eliminate the shear and transverse stress components when the hoop stress is decomposed into the material coordinate system. The shear and transverse strength of fiber composites are matrix dominated and are very low compared to the fiber direction. Once formed and dried, the tube was sectioned and then tested.

(G) *Composite test sample analysis*.

The test samples generated and tested are shown in Figure 16. Again, the C-fiber with resin and nanofiller were investigated due to the lack of interaction presented in Figure 3. Three samples were successfully generated and analyzed for the: (a) naked nanoparticle, (b) TiO_2-NW coated with APTMS, and (c) TiO_2-NW coated with MCPA._ For each of these samples a 3-point test was performed. Once broken, the test samples were analyzed by SEM. The figures obtained are shown in Figure 16. As can be observed, the samples visually show clustering of the nanofiller (white dots).

The interlaminar shear strength of the carbon fiber composites was found to improve upon addition of the TiO_2 nanoparticles compared to the carbon fiber composite without nanoparticles (Figure 17). The impact was greatest for the unfunctionalized TiO_2 where the interlaminar shear strength was increased by 33%. When evaluating the quality of the dispersion and of the fiber wind with an optical microscope, the TiO_2 were found to have agglomerated and phase separated from the resin (Figure 18). The agglomerated particles disrupted the packing of the fibers. It was expected that the void created by particle agglomerates in the fiber packing would act as a defect and a stress concentration region resulting in a lower interlaminar strength.

The 3-point-bend results show the opposite effect by an improved interlaminar strength, more pronounced for the unfunctionalized TiO_2. The mechanism behind the improvement is presently unknown.

Figure 16. (LEFT) Carbon fiber composite arch samples without (A) and with (B,C) nanoparticles. (RIGHT) Arch composite sample shows interlaminar shear fracture in the center of the sample after testing by 3-point-bend.

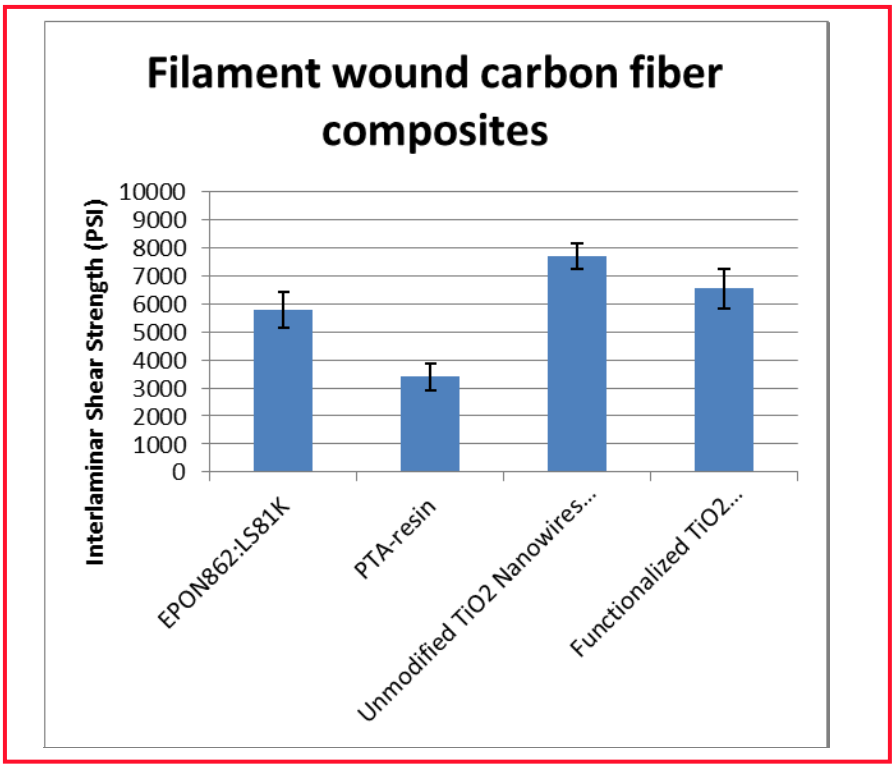

Figure 17. The interlaminar shear strength of filament wound carbon fiber arch samples as measured by 3-point-bend for the sample with (A) no nanoparticles, (B) unfunctionalized TiO_2 nanoparticles, and (C) functionalized TiO_2 nanoparticles.

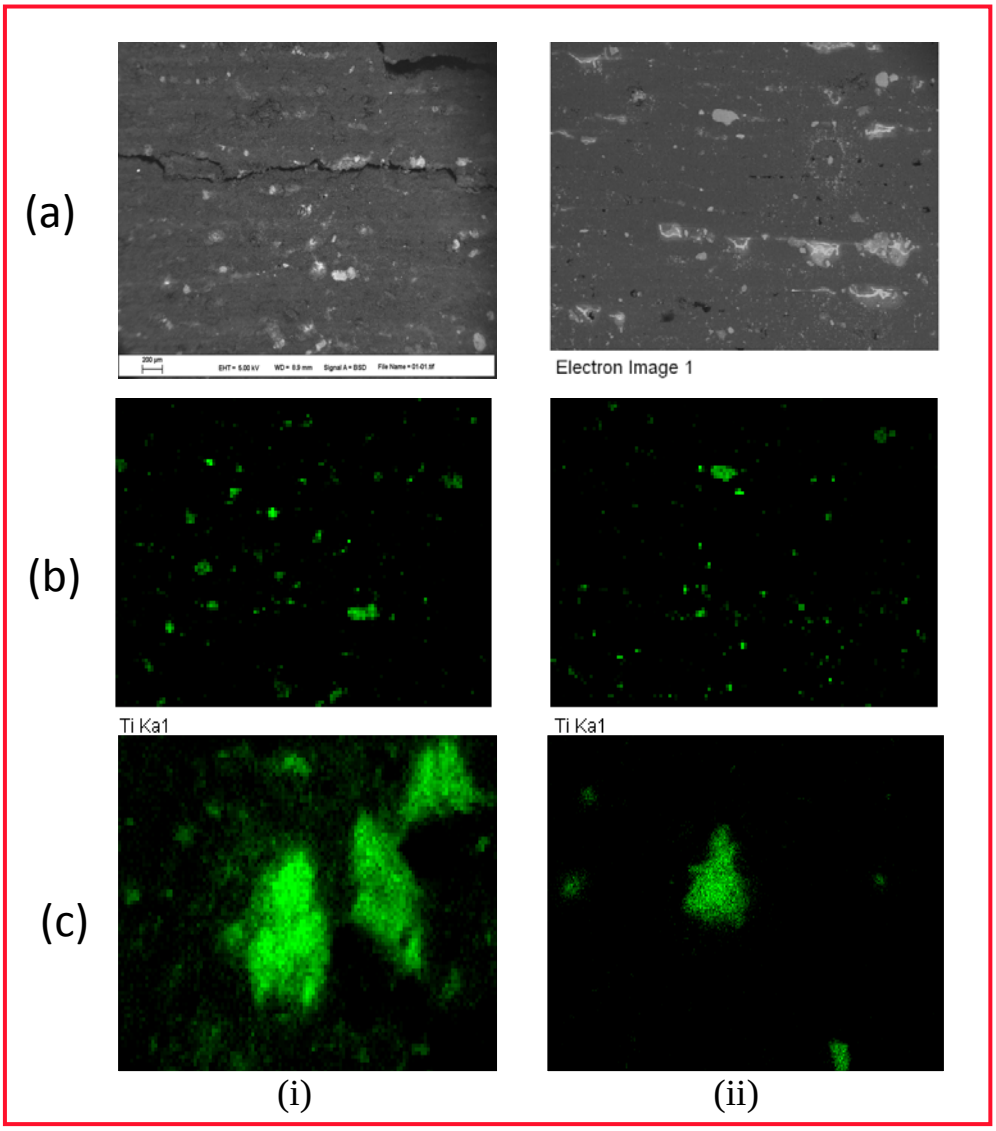

Figure 18. Nanoparticle filled resin (i) sample B, (ii) sample C: (a) Optical images of nanoparticle filled sample, (b) TEM images with TiO_2 mapped, (c) higher magnification of TiO_2 mapping.

4. ECONOMIC ASSESSMENT OF IMPROVED NANOCOMPOSITES

To evaluate the improved nanocomposites as used in Beacon flywheels, a standard economic evaluation technique was employed that starts with life-cycle cost analysis and extends it to accommodate additional economic measures of importance to this flywheel analysis. Life-cycle cost analysis (LCCA) is the analytic process of assessing the costs (and revenues, or negative costs) that occur over the intended life of a structure or set of assets. Most LCCA frameworks follow a specific set of steps, conditions, and requirements to produce economic assessments of the most value to stakeholders. The analysis herein follows *ASTM Standards on Building Economics*,[26] an industry-standard document that describes steps for life-cycle cost analysis, benefit-cost analysis, savings-to-investment calculations, net-benefit analysis, and uncertainty and sensitivity analysis. These economic approaches, for example, are used within the Department of Energy to estimate the economic costs, benefits, and other factors of building- and energy-related decisions.[27]

The essential components of this and most other LCCA frameworks include an *agency* that considers owning or using a particular set of assets that will perform some specific function over their intended *functional life.* For example, a power company can consider a flywheel energy storage system for use in grid-scale battery systems, such as the installation in Stephentown, NY. This agency explicitly or implicitly needs to compare the best of competing *alternate decisions*, most often composed of a *base case* (or "do nothing" strategy) and a new, alternate strategy. For example, a battery company's 'do-nothing' strategy would be to install flywheels with the existing composite structures, maximum angular velocities, and associated energy storage capacities. The alternate strategy would be to implement an improved-

nanocomposites flywheel of higher capacity (and cost). While based on engineering or other functional data these assets may operate for a very long time, there is an *analysis or study period* over which the agency is interested in analyzing benefits and costs. For example, a flywheel battery system may last 60 years due to excellent design and careful maintenance, but for planning purposes an energy storage supplier may only want to consider costs and benefits over the next 20 years. Costs (and revenues) that occur in different years of this analysis period need to be compared, specifically through their summation over the study period. A number of factors change costs and revenues over the study period of an asset:

a. the costs of constructing the alternates - the improved-nanocomposites flywheel in particular has *new-technology* costs associated with modifying, testing, and implementing the new design, along with the additional costs of the new wheel, if it is more expensive;

b. the revenues generated by the asset, in this case in regulation service markets;

c. the changes in the prices of labor, capital, and materials to conduct operation, maintenance, and repair (OM&R) of the asset; and

d. the time value of money.

Within this framework, the benefits of a particular alternate are typically negative costs, i.e., they reduce the costs associated with a particular alternate. To make the two sets of costs directly comparable, they need to be converted to equivalent values for a *base year*, which is typically the first year of the study period. The formula used to estimate *constant-dollar, life-cycle cost* is the following formula, based on a nomenclature where t is the particular year within the study period of T years, $\{c_t\}$ is the set of costs that occur in year t, i is the average *inflation rate* over the study period, and r is the average *nominal discount rate*, which includes the time value of money and inflation:

$$LCC = \sum_{t=0}^{T} \sum_{\{c_t\}} c_t \left(\frac{1+i}{1+r} \right)^t \qquad (6)$$

Often with energy-related projects, different costs will have different inflation rates, e.g., for the increase in electricity rates ($/MWh) versus the increase in OM&R costs. Ultimately, when comparing the life-cycle cost (LCC) of two alternate strategies or decisions, the one with the lowest LCC is the *cost-effective alternative.*

While LCCA quantifies all costs and benefits associated with alternate strategies in dollar terms, thereby making direct comparison straightforward, there are useful groupings of costs and benefits that lend to analytical comprehensiveness and economic insight. Following Ehlen,[28] costs can be grouped into three distinct, non-overlapping, and ultimately additive types:

1. *Agency* costs and benefits, which are the costs to the agency that owns, maintains, and/or has economic decision authority over the set of assets. These are typically market-based, i.e., they involve explicit transactions in the marketplace. Example: the costs and benefits of a faster flywheel and resulting energy storage capacity to an energy storage provider.

2. *Non-agency* costs and benefits, which are to entities that are not the direct owner(s) of the assets but use them directly. These are typically non-market based, or external in nature. Example: the costs and benefits to transmission operators who better use grid components for power stabilization.

3. *Third-party* costs and benefits, which are to entities that are neither owners nor direct users of the assets. These costs are typically non-market based, or external in nature. Examples: costs and benefits to humans who benefit from reductions in carbon emissions and green-house gasses caused by the reduction in generation capacity normally required for grid stabilization.

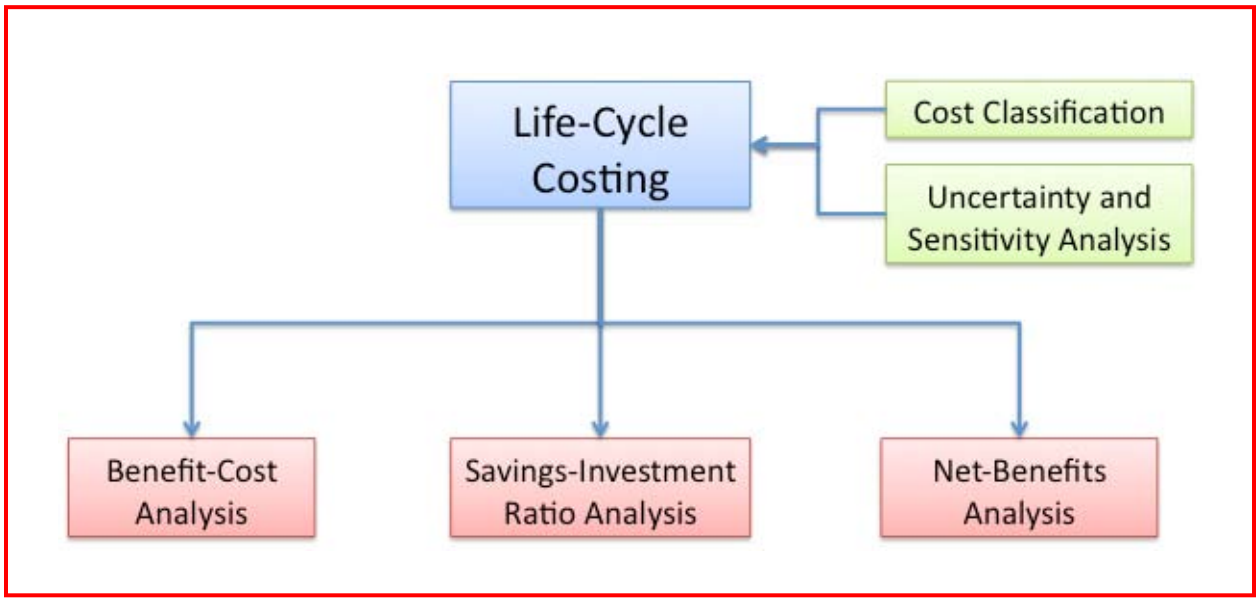

Figure 19. Structure of Economic Analysis Components

Agencies then have the ability to compare and weigh the relative merits of alternatives based on their effects on the agency, on those that use the alternatives, and all others. As illustrated by this LCCA approach in Figure 19 and associated classification scheme, this provides a foundation for conducting benefit-cost analysis, net benefits analysis, savings-investment ratio analysis, and uncertainty and sensitivity analysis. The approach taken in addressing the impact of the flywheel improvements (*vide infra*) are discussed below: *A. Benefit-Cost Analysis* , *B. Analysis Process*, *C. The Economic Assessment*, *D. Life cycle costs*, and *E. Assessment of Improved-Nanocomosites Technology*.

A. Benefit-Cost Analysis. Benefit-cost analysis uses the LCCA framework and calculations to directly calculate and compare the costs and benefits associated with an alternate vis-à-vis the base case. The net relative benefits of the alternative (its benefits minus any benefits of a do-nothing base case) are compiled using equation 6 and then compared to the net relative costs (its

costs minus any costs of a do-nothing base case, using equation 7 and used to compute the benefit-cost ratio.

$$\text{Benefit - cost ratio} = \frac{B}{C} = \frac{\sum_{t=0}^{T}\sum_{\{b_t\}} b_t\left(\frac{1+i}{1+r}\right)^t}{\sum_{t=0}^{T}\sum_{\{c_t\}} c_t\left(\frac{1+i}{1+r}\right)^t}. \quad \textbf{(7)}$$

The advantage of this approach includes that it uses the same set of costs and benefits used to compute life-cycle cost (equation 6). If this B-C ratio is greater than one, the alternate is the cost-effective strategy.

Savings-investment ratio analysis uses the LCCA framework and calculations to estimate the savings associated with an alternative and compare them to the investment required to implement the alternate strategy. The savings of an alternative (its relative costs and benefits when compared with a base case, do-nothing strategy) are compared with the costs of investing in the alternate strategy, again using some or all of the data used in equation 6 and used to compute the savings-to-investment (SIR = S/I; where S = savings and I = investment) ratio. If the S/I ratio is greater than one, the alternate is the cost-effective strategy.

Three important follow-on analyses should be included in a life-cycle cost analysis: factor analysis, uncertainty analysis, and sensitivity analysis. Factor analysis provides insight into which parts of the data and overall model are the largest contributing factors to overall life-cycle cost. For example, in an energy storage system analysis, it's important to know whether the service load prices (i.e., cost of electricity), system installation costs, or new technology costs are the largest factors driving life-cycle cost.

Second, with any analytical model or process there can be considerable uncertainty in the data, models, and associated parameters used. For example, in the above life-cycle costing and

derivative calculations, there can be uncertainty in the appropriate study period, the expected life of the assets, the construction, new-technology and OM&R costs, the inflation rate, and real discount rate. Furthermore, in the case of a grid-scale energy storage system, there is considerable uncertainty regarding future electric service load rates. This uncertainty can affect the analytical conclusion of whether or not implementing an energy storage system is a cost-effective strategy. Qualitatively speaking, *uncertainty analysis* provides a means for assessing the effects of data uncertainty (i.e., whether the data are correct) on the analytical results, and *sensitivity analysis* provides a means for assessing the effects of model uncertainty (i.e., whether the model is correct) on the analytical results.

Uncertainty analysis is conducted after completion of the LCCA and associated benefit-cost or other metrics. The "best-estimate" values of cost and associated LCCA parameters were used and initial assessments of life-cycle cost-effectiveness were made. For uncertainty analysis, the analyst makes assessments of the uncertainty in these underlying parameters, and then re-calculates life-cycle cost and the associated measures using these variations in parameters. If these re-calculations indicate the particular strategy is still the cost-effective strategy, then the analyst can conclude that this strategy is robust or insensitive to variations in these data and parameters.

Finally, sensitivity analysis is used to determine if and how the calculations are sensitive to particular parameters or subsets of parameters. This sensitivity can be calculated, for example, by computing the changes in the LCC and other cost measures caused by a 1-percent change in the data or parameter value. If the LCC and other computations are very sensitive to one or more of these parameters, then further more detailed analysis of this parameter and model may be warranted.

B. Analysis Process. Benefit-cost analysis and the supporting life-cycle cost calculations require a specific set of inputs, are conducted using specific set of steps, and generate specific results. To conduct life-cycle costing and related analyses, the analyst needs to provide the following information:

1. A statement of the **functional goal** and ***performance requirements***[29] of this goal, i.e., "provide an estimated 5000 hours of area regulation services to the power grid in Stephentown, NY. The power capacity should be in the range of 20 MW to 26 MW.

2. A list of the **alternate strategies used to meet these goals**, including (1) a base case or "do nothing" strategy, e.g., a Stephentown, NY-class flywheel system; and (2) an alternate strategy, e.g., using improved nanocomposites in the Stephentown-class flywheel.

3. A **study period** over which the alternates will be evaluated, say 20 years.

4. "Best-guess" estimates of the costs associated with, where applicable, the construction, operation, maintenance, repair, and sometimes removal of the alternatives over the study period. These costs are typically provided in terms of what they would cost today to do, not in the year(s) in which they occur.

5. "Best-guess" estimates, where applicable, of the benefits associated with activities that occur due to the alternate in question, over the study period. As with costs, these benefits are typically quantified in terms their value today, not their value in the year(s) in which they occur.

6. Who pays the costs and who receives the benefits, using the classification scheme in Section 0.

7. to estimate the total benefits, and use the "best guess" costs of each alternative.

Once prepared, the analyst uses the "best-guess" costs and benefits of each alternative to compute the life-cycle cost of each alternative, where the set of costs (including benefits as negative costs) is computed using **Error! Reference source not found.**. The alternate with the lowest LCC is the cost-effective strategy. The "best-guess" benefits of each alternate vis-à-vis the base case is used to estimate the total costs and then use **Error! Reference source not found.** to compute the benefit-cost ratio of that alternate vis-à-vis the base case. The alternate with the highest B-C ratio (greater than 1) is the cost-effective strategy among all alternatives

(including the base case). If none of the B-C ratios are greater than one, the "do-nothing" alternative is the cost-effective alternative.

C. The Economic Assessment. Following the steps outlined above, we conducted a preliminary, illustrative analysis of the potential benefits and costs of improved nanocomposites as used in the Beacon flywheel. While some of the steps herein may appear superfluous or an over-complication of an otherwise straightforward economic analysis, they are provided as examples of how the approach can provide a simple, standard structure for conducting more comprehensive analyses of energy technologies. There are many potential market and non-market costs and benefits associated with improved flywheel performance. These costs and benefits can be to agencies, non-agencies, and third parties. This preliminary analysis, however, considers only the market-based agency costs and benefits; future analysis could include these other types of costs and benefits.

The performance requirements for our alternate strategies are based on the current specifications of the Beacon Power Company in Stephentown, NY: to provide area regulation services on an as-needed basis. Table 4 provides a summary of the baseline performance parameters for our analysis.

Table 4. Performance Parameters: Beacon Power Company

Item	Value	Source
Area regulation: discharge duration	15 min.	Eyer and Corey (2010), p. 24.
Estimated annual service hours	5,000	Eyer and Corey (2010), p. 24.
Market regulation rate ($/MW per service hour) = revenue	$40.00	Eyer and Corey (2010), p. E-4
Utilization rate (%)	50%	
Roundtrip efficiency (%)	81%	Eyer and Corey (2010), p. E-4
Plant Uptime	95%	Eyer and Corey (2010), p. E-4

Area regulation service provides the ability to manage variations in frequency that degrade the performance of components and the overall power grid. Area regulation services control these frequency variations by removing relatively small amounts of energy from the grid and then returning them, at small time intervals. Generally speaking, the faster it can remove/return energy, the better the frequency control. The stored energy plan generates revenue based on the number of hours it functionally is asked to and it carries out regulation services. As listed in the table, 15 minutes of discharge duration means that it can discharge stored energy for a maximum of 15 minutes. The estimated service hours in the table are the expected number of hours that the flywheel system will provide regulation services to the grid in a given year. The *market regulation rate* is the sum of up and down rates. Annual market revenues are calculated using the annual service hours, utilization rate, roundtrip efficiency, and plant uptime. The *utilization rate* is the fraction of capacity that is used for these service hours, and the plant uptime is the fraction of overall calendar time that the system is used, i.e., the system will need to be down for an estimated 5 percent of the time, e.g., for maintenance and repair.

Two alternate strategies were considered to meet the performance requirements of a grid-scale BESS contributing to regulation services market:

- **Base case:** a "do nothing" strategy, where the current energy storage capacity is 5 MWh and power capacity is 20 MW, and

- **Alternative 1:** an improved energy storage capacity of 6.5 MWh and power output of 26 MW, or 30 percent over the current Stephentown capacity, based on improved-nanocomposites flywheels. (This all assumes that the power rating can go up with the energy storage capacity.)

Key differences in these alternatives are shown in Table 5.

Table 5. Project Alternatives and Properties

Item	Property	
	Base Case	**Alt. 1**
Increase in angular velocity vis-à-vis existing Beacon flywheel	-	14%
Increase in energy storage vis-à-vis existing Beacon flywheel	-	30%
Energy storage capacity (MWh) / Power rating (MW)	5 / 20	6.5 / 26

The standard costs associated with the alternatives considered include

- Flywheel system installation costs – these are essentially the "purchase price" of an existing 20-MW Beacon BESS system as used in the Stephentown, NY facility;

- "New-technology" costs associated with the improved nanocomposites – these include the cost of Sandia applied research in this area, and implementation and testing by Beacon Power Company, and the additional cost of the improved wheel and higher power output electronics; and

- Annual flywheel system operation, maintenance, and repair costs.

The benefits associated with the improved nanocomposites considered include

- Increased revenue due to increased energy storage and power capacity, all else assumed equal.
-

Table 6 lists the parameters and their best-estimate values (and sources) used to compute the costs and benefits associated with the two alternatives. Two forms of inflation were used in the

analysis: the change in prices of energy and the change in the average price of all goods. These two rates can differ significantly and since the primary costs herein are energy related, their change over time should be accurately assessed.

Table 6. Best-Estimate Parameter Values

Parameter (Unit of Measure)	Best Estimate	Source
Avg. Annual Incr. in Service Load,(%/yr)	1.00%	DOE EIA [a]
Stephentown, NY "Overnight Cost" ($)	$43,000,000	DOE,[b] KEMA[c]
New Technology Costs of Improved Nanocomposites	$4,000,000	assumption
Increase in Flywheel Capacity due to Improved Nanocomposites	30 percent	Boyle assumption
Annual Operation Maintenance Cost ($/yr)	$100,000	
Service Load Price Inflation (%/yr)	1.90%	DOE EIA[d]
Real Discount Rate (%/yr)	2.30%	OMB Circular A-94
Inflation Rate (%/yr)	1.90%	OMB Circular[e]

(a) We proxy the annual increase in service load over the twenty year period with the average increase in electricity demand, which can be found at: U.S. Department of Energy, U.S. Energy Information Administration, "Forecasts and Analysis of Energy Data," accessed at http://www.eia.gov/oiaf/forecasting.html on July 30, 2012. How is this used? (b) U.S. Department of Energy, "Department of Energy and Beacon Power Finalize $43 Million Loan Guarantee for Innovative Energy Storage Project New York State," accessed at http://energy.gov/articles/department-energy-and-beacon-power-finalize-43-million-loan-guarantee-innovative-energy on July 30, 2012. (c) KEMA, Cost Comparison for a 20 MW Flywheel-based Frequency Regulation Power Plant, KEMA Project : 0003.002, September 2007, Table 1 p. 14. At the listed $1,630 / kW, the plant would cost 1630 x 20,000 kW = $33 million. (d) We proxy the average-annual increase in service load prices with the DOE forecast average annual increase in general electric energy prices, found at op cit, DOE "Forecasts and Analysis of Energy Data." (e) The average annual inflation rate that is consistent with the OMB circular's nominal and real discount rate can be computed as: inflation rate i = [(1 + n) / (1 + r)] – 1, where n = the nominal discount rate and r = the real discount rate.

D. Life cycle costs. While there are a number of measures of cost-effectiveness listed in Section A, we compute only two of them: life-cycle cost and benefit-cost ratio. Life-cycle costs were computing using an Excel spreadsheet and the values in Table 4-6. Base Case life-cycle cost was computed as the discounted present value of annual

i. Annualized capital cost + flywheel OM&R costs – annual revenues. Alternative-1 life-cycle cost was computed as the discounted present value of annual

ii. *Annualized capital cost + New technology costs + flywheel OM&R costs – annual revenues.* OM&R costs were inflated using the general inflation rate. The nominal interest rate was then used to compute the present value of these future, inflated costs. If revenues are greater than costs, then life-cycle costs are negative, i.e., the baseline BESS alternative is profitable.

The LCC of each alternative is then the present value of each cost. Table 7 lists their values, rounded to the nearest $1 million. The system with improved nanocomposites, with a life-cycle cost of (negative) $7 million (that is, a negative cost due to positive revenues), is the cost-effective alternative between our two alternatives. Figure 20 shows the same information in graph form, where the numbers are listed as positive values. Figure 21 in particular gives a breakdown of the revenues and costs (in discounted present value form) for each alternative: comparing the two alternatives, the Alternative 1 Nanocomposites have slightly higher costs (due to new-technology costs) but significantly higher revenues (due to the higher capacity).

Table 7. Life-Cycle Cost, by Alternative

Alternative	**Life-Cycle Cost**
Base Case - 20 MW Capacity	$3 million
Alternative 1 – 26 MW Capacity	($7 million)

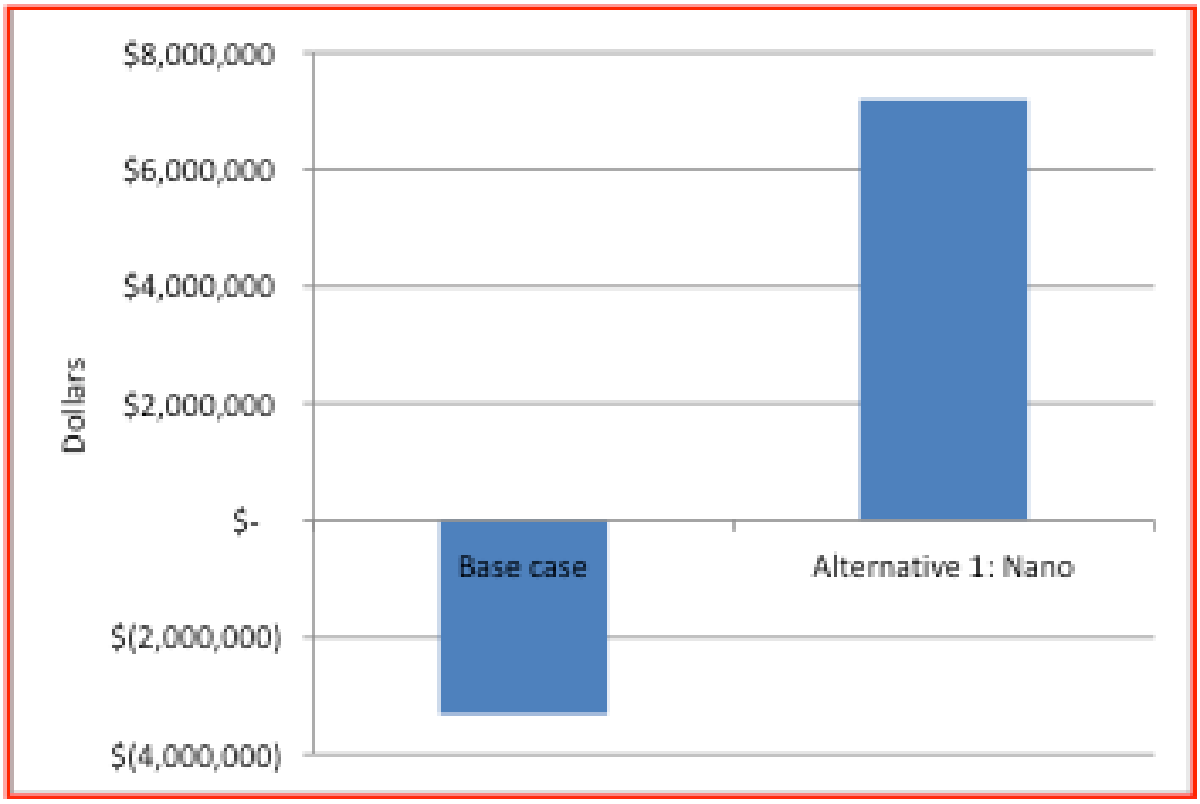

Figure 20. Life-Cycle Cost (Negative), by Alternative

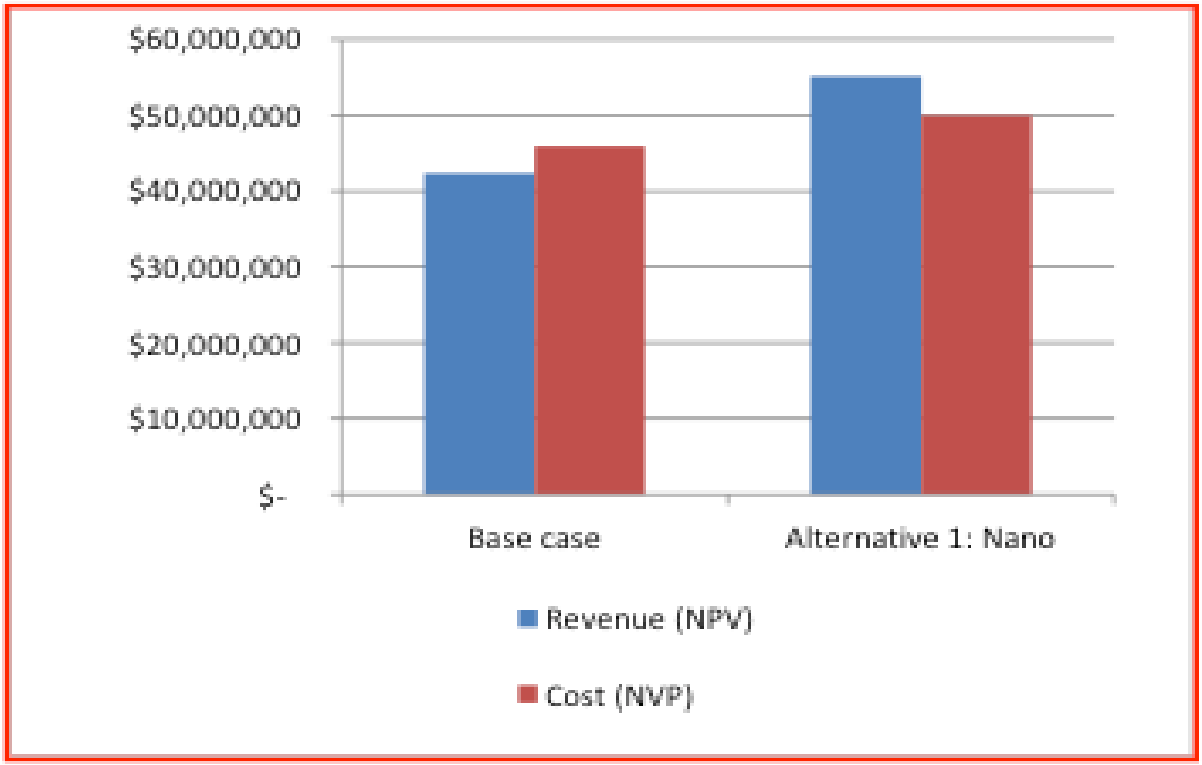

Figure 21. Revenues and Costs, by Alternative

Fig

ures 22 and 23 give more information on profitability, in terms of discounted revenues and costs, by year. Figure 24 shows the difference between revenues and costs (in discounted present value), by year and alternative. Based on our current assumptions, the Base Case has negative annual net revenue in the early years, until demand and market rates escalate sufficiently to generate positive net revenue. (As described above, we assume that that the demand for regulation services will increase with future baseline demand and market energy rates, but others estimate that regulation service demand will increase due to future changes in

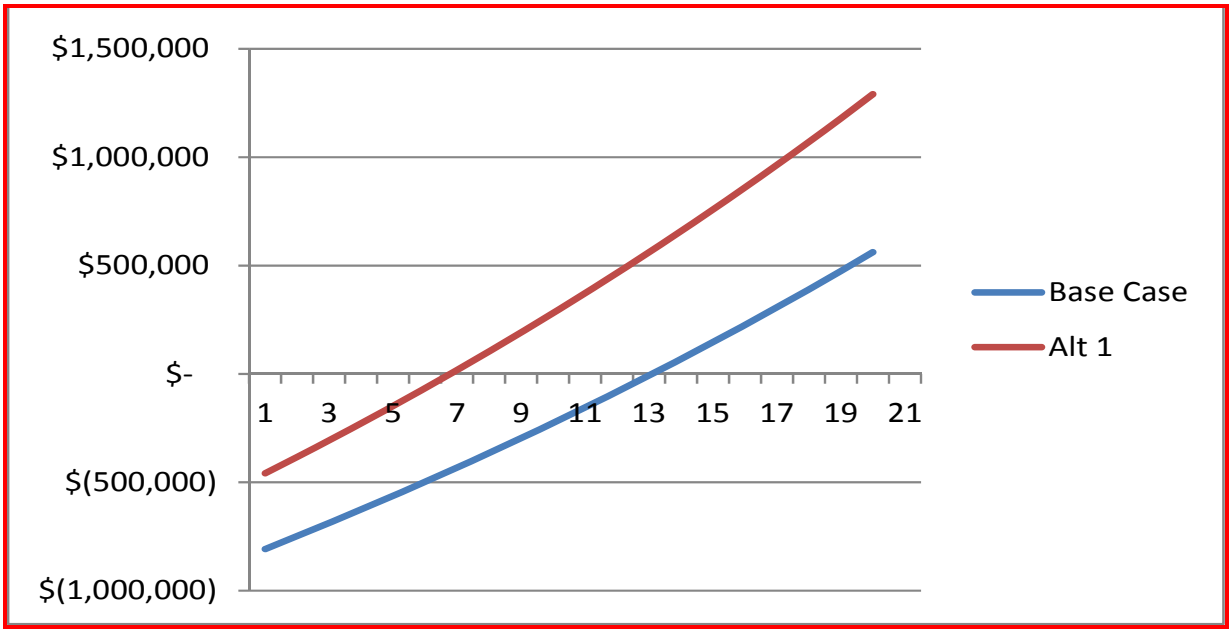

Figure 22. Annual Costs (Discounted Present Value), by Year and Alternative

the structure of the energy production, transmission, and distribution). Figure **23**, which shows cumulative values of the same variables, illustrates how the Base Case does not have positive cumulative net revenues, or returns, until about Year 10 of the 20-year study period. The Alt 1 (nanocomposites) alternative has positive net revenue by Year 12, due to the higher market revenues (caused by the higher energy storage capacity) being greater than the higher installation

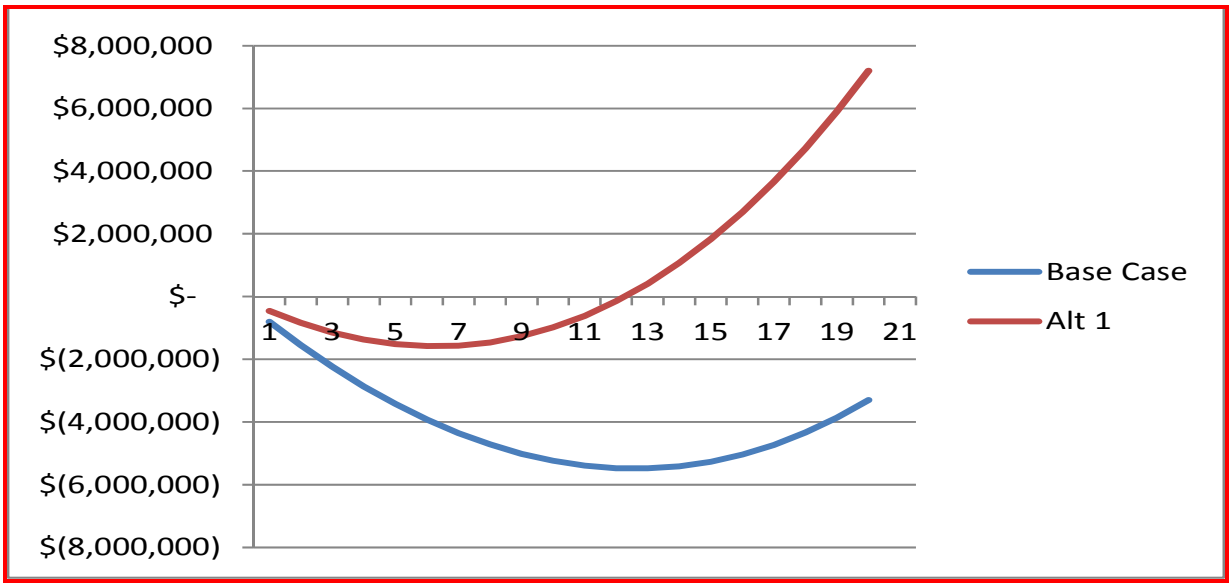

Figure 23. Cumulative Costs (Discounted Present Value), by Year and Alternative

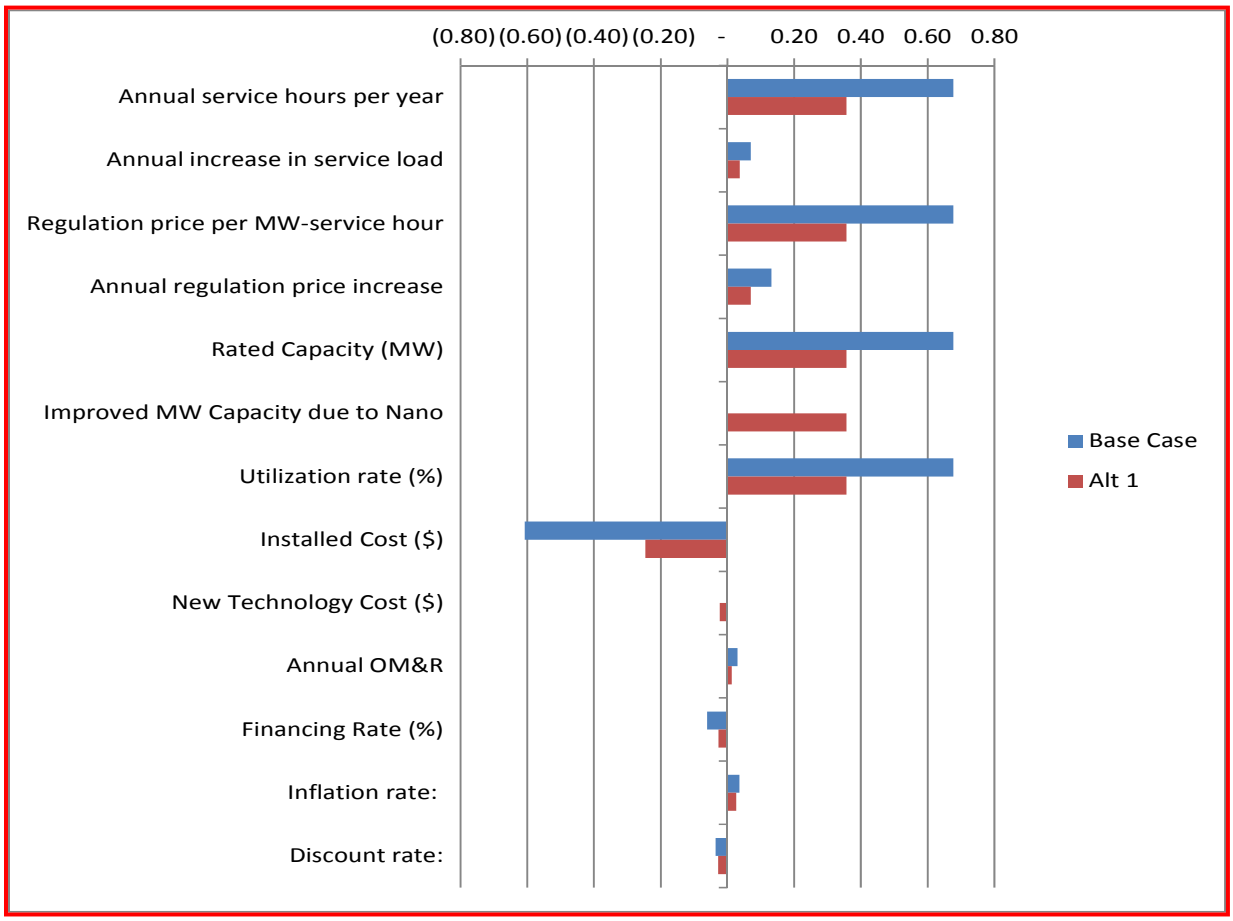

Figure 24. Effects 10-Percent Change in Parameter Value on Life-Cycle Cost

costs (caused by the nanocomposites new-technology costs).

Given the two alternatives, we computed a benefit-cost (B-C) ratio for the alternative flywheel vis-à-vis the base case "do nothing" flywheel. Benefits are computed as net additional market revenues from the improved-nanocomposites BESS. The costs of the alternative are the additional new-technology costs. Table 8 lists the individual values, the sums of costs and benefits, and the resulting benefit-cost ratio of 3.1. Given that the benefit cost ratio is greater than 1, the improved-nanocomposites BESS is the cost-effective alternative.

Table 8. Benefit-Cost Ratio Calculations: Improved-Nanocomposities Flywheel

Benefits (Increased Revenues)	$12,700,000
Costs (New Technology Costs)	$4,100,000
Benefit-Cost Ratio	**3.1**

Finally, we can compute the annual return on investment of implementing the improved nanocomposites flywheel design. Table 9 lists the ROI calculations based on our assumed parameter values.

Table 9. Return on Investment: Improved Nanocomposites Design

Return	$12,700,000
Investment	$4,100,000
ROI	311%
Annual ROI	**6%**

The investment cost of the improved nanocomposites design is an estimated $4 million, which reflects the new technology costs of applied research, implementation and testing. The return on this investment, over the 20-year study period, is an estimated 300 percent, or 6 percent per year. Given that these results may be sensitive to the underlying parameters used, for example, in Table 6, we need to conduct some uncertainty analysis to see under what conditions our results

are robust to changes in the performance characteristics of the improved-nanocomposites flywheel and in the economic profitability of the flywheel installation. To do that, we conduct some basic sensitivity and breakeven analysis. Sensitivity analysis allows us to determine which parameters have the greatest influence on the calculated life-cycle costs and other measures of cost-effectiveness of the improved-nanocomposites flywheel; breakeven analysis allows us to effectively determine the boundary parameter values for cost effectiveness. This effect is illustrated by our sensitivity analysis of our LCC model for the Base Case and Alternative 1 strategies. For each of the parameters listed in Table 6, we increased its value by 10 percent and then computed the percent increase in life-cycle costs of each alternative.

As illustrated in Figure 24, the life-cycle costs of the Base Case and Alt 1 are most sensitive to changes in the annual service hours, the regulation price, the rated capacity, the utilization rate, and the installed cost. For each parameter, a 10-percent increase in its value increases the life-cycle costs of the Base Case and Alt 1 by 60-percent and 40-percent, respectively. Changes in the other parameters, on the other hand, had relatively little effect on life-cycle costs. Table 10 lists the results of the breakeven analysis. For a subset of the analysis parameters, we calculate the value at which (a) the base case becomes profitable and (b) the alternative 1 improved nanocomposites case is no longer profitable. These values help us "bound" the cases of cost-effectiveness of the two alternatives.

Table 10. Breakeven Analysis

Breakeven Values	Base Case	Alt 1
Annual service hours per year	5,200	4,400
Annual increase in service load	1.8%	-0.1%
Regulation price per MW-service hour	43	35
Annual regulation price increase	2.3%	0.5%
Rated Capacity (MW)	22	18
Improved MW Capacity due to Nano	-	1.15
Utilization rate (%)	55%	45%
Installed Cost ($)	40,000,000	53,000,000
New Technology Cost ($)	-	10,000,000
Financing Rate (%)	1.50%	3.5%

In the case of the Base Case, this strategy makes economic sense for very minor changes in the modeling assumptions. For example, the Base Case is profitable if the annual service hours increase to 5,200; if the annual increase in service load increases to 1.8%; if the base-year regulation price increases to $43; and so on. In the case of the Improved Nanocomposites alternative, it has positive net present value unless the annual service hours decrease to 4,400 per year; if the service load decreases annual by 0.1%, and the improved MW capacity is as low as 15 percent, and so on.

E. *Assessment of Improved-Nanocomosites Technology*. The above calculations provide good initial estimates that can be used to discuss the relative benefits of the improved nanocomposites. As mentioned above, we are specifically economically evaluating the economic benefits and costs associated with improving the Beacon flywheel energy storage capacity vis-à-vis the design in the Stephentown, NY facility.

Using the assumptions herein, the following assessment are made. The 20-MW baseline flywheel energy storage system costs an estimated $2,000 per kW power capacity and $8,000 per kWh energy storage capacity, based on the $43,000,000 installation cost. Taking into account the

increased performance but also increased, new-technology costs, these costs are reduced to $1,650 per kW (or 20 percent) and $6,000 per kWh (or 25 percent), respectively. In addition, the plant's revenues, effectively its return on the improved-nanocomposites investment, increase by 30 percent. Given that the marginal investment is $4 million in new technology costs (research, development, implementation, and testing), the return on investment is approximately 300 percent, or 6 percent annually, over the 20-year study period. Further, the improved-nanocomposites flywheels spin 14-percent faster than the current Stephentown "Gen4" flywheel. Given that there have been at least two flywheel failures early at the facility,[30] there is some risk of additional costs and reduced capacity of the facility, at least in the shorter term, when additional testing and other new-technology costs could increase. But as shown in the breakeven analysis and sensitivity analysis sections, there is sufficient room for the in-the-field flywheel improvements, due in part to the large increase in output capacity and the less-than-full capacity utilization (50 percent) assumed for this particular project. All else being equal, a marginal additional cost of $100,000 per year for increases in flywheel failures still gives the improved-nanocomposites design a benefit cost ratio of 2.1 and a return on investment of 200 percent or 4 percent per year.

Our initial calculations are based on "best estimates" of a large number of performance and economic assumptions that have not been verified in the field; these include the actual number of service hours the facility would generate revenues from, the market rates, the utilization percentage, and so on. (Our revenue estimates, however, do closely match a quarterly revenue report of $525,000,[31] which annually would be $2 million, as listed in the table in revenues and cost calculations in Appendix A). In fact, the preliminary estimates suggest that the current Stephentown facility is not profitable based on our best estimates. The improved-nanocomposites

design, however, is profitable under these same assumptions, and thus significantly more likely to be profitable under the range of potential grid applications, market prices and other conditions, and long-term deployment over a range of possible grid locations. That is, from a business-strategic standpoint, the improved-nanocomposites design is a significantly better business proposition. There are a number of significant advantages of the improved-nanocomposites design and the Beacon flywheel overall, suggesting that further investments in this particular battery technology are strategically important; these include:

a. As compared with, for example, chemical-energy batteries, kinetic energy flywheels are low- to no-emission, sustainable[32] technologies. Strategically, their long-term potential for future obstacles created by, say, environmental or critical-material concerns are very low.

b. The component structure of the individual flywheel units of the "pods" of 20 flywheels, and the overall Stephentown component make the flywheel system easy to maintain, to replace components, and to transplant flywheel components on an as-needed basis. This flexibility allows private companies operating them to manage strategic business risks more easily versus larger, fixed power assets.

c. A 30-percent improvement of an existing, proven technology is strategically less risky than, say, a 30-percent improvement from a yet-to-be-proven technology.

According to Eyer and Corey (2010), there is an estimated 1 GW capacity for area regulation services over the next ten years. That is, enough demand for regulation services that 50 Beacon flywheel BESS systems could be installed. Using EPRI estimates of ranges of ESS costs,[33] 20% decrease in $/kW and $/kWh costs makes flywheels near competitive with Li-ion batteries ($1085-$1550/kW, $4340-$6200/kWh), but not advanced lead-acid.

5. CONCLUSION

The investigation of ceramic nanofillers were found to increase the final strength of a test specimen by more than 30% in comparison to standard setups. This study produced a large scale preparative route to TiO_2 NW. These nanofillers were successfully functionalized with silanes and their properties determined within the various resin systems. Based on these results, we successfully incorporated the TiO_2 NW in the resin. Using the optimize functionalization to determine novel cure, fillers, and alternative processing, prototype manufacturing of test specimens was realized. The test specimen were evaluated using a 3-point bend test on sections of the 4" mockup. The mechanical response of these test specimen were used to develop constraints and develop laboratory-based methods to measure and predict critical mechanical features in large-scale nanocomposites. The results indicated a 30% increase in the strength of the test sample in comparison to a standard mock-up was achieved. Interestingly, the TiO_2 NW in these samples were found to poorly distributed, with clusters of TiO_2 noted in the SEM images. Additional work to improve the distribution are underway, followed by test sample analyses.

An economic impact of the improvement noted above was conducted. Based on an increased shear and interlaminar-fracture strength of flywheel carbon fiber-epoxy composite by 30%, a 20-30% reduction in flywheel energy storage cost ($/kW-h) may be enabled. This technological improvement may increase power capacity to 26 MW and energy capacity to 7.5 MW-service hours. This will decrease the average energy storage costs to $1500/kW and $6000/kW-h. After accounting for new-technology and additional production costs, return on improved-nanocomposite investment is 4%-6% per year over 20-year service life.

Further work is underway to disperse the nanofiller ceramic and carbon wires evenly throughout the resin in order to garner the greatest impact. Once this is determined, the optimal nanofillers will be used to build mock flywheels and test their spin strengths/speeds.

6. REFERENCES

(1) Lan, Y. F.; Lin, J. J. *J. Phys. Chem. A* **2009**, *113*, 8654.

(2) Peeterbroeck, S.; Alexandre, M.; Nagy, J. B.; Pirlot, C.; Fonseca, A.; Moreau, N.; Philippin, G.; Delhalle, J.; Mekhalif, Z.; Sporken, R.; Beyer, G.; Dubois, P. *Compos. Sci. Tech.* **2004**, *64*, 2317.

(3) Sun, D.; Chu, C.-C.; Sue, H.-J. *Chem. Mater.* **2010**, *2*, 3773.

(4) Tang, C. Y.; Xiang, L. X.; Su, J. X.; Wang, K.; Yang, C. Y.; Zhang, Q.; Fu, Q. *J. Phys. Chem. B* **2008**, *112*, 3876.

(5) Li, S.; Wang, F.; Wnag, Y.; Wang, J. W.; Ma, J.; Xiao, J. *J. Mater. Sci.* **2008**, *43*, 2653.

(6) Vassileva, E.; Friedrich, K. *J. Appl. Polym. Sci.* **2006**, *101*, 4410.

(7) Cheng, L.; Zheng, L.; Li, G.; Zeng, J.; Yin, Q. *Physica B.* **2008**, *403*, 2584.

(8) Chau, J. L. H.; Tung, C.-T.; Lin, Y.-M.; Li, A.-K. *Materials Lett.* **2008**, *62*, 3416.

(9) Li, Y.-Q.; Fu, S.-Y.; Yang, Y.; Mai, Y.-W. *Chem. Mater.* **2008**, *20*, 2637.

(10) Nyman, M.; Shea-Rohwer, L. E.; Martin, J. E.; Provincio, P. *Chem. Mater.* **2009**, *21*, 1536.

(11) Akinyede, O.; Mohan, R.; Kelkar, A.; Sankar, J. *J. Composite Mater.* **2009**, *43*, 769.

(12) Kane, M. C.; Londono, J. D.; Beyer, F. L.; Brennan, A. B. *J. Appl. Cryst.* **2009**, *42*, 925.

(13) Guo, Z. H.; Pereira, T.; Choi, O.; Wang, Y.; Hahn, H. T. *J. Mater. Chem.* **2006**, *16*, 2800.

(14) Hong, R. Y.; Fu, H. P.; Zhang, Y. J.; Liu, L.; Wang, J.; Li, H. Z.; Zheng, Y. *J. Appl. Polym. Sci.* **2007**, *105*, 2176.

(15) Boo, W. J.; Liu, J.; Sue, H. J. *Mat. Sci. Tech.* **2006**, *22*, 829.

(16) Sarwar, M. I.; Zulfiqar, S.; Ahmad, Z. *J. Sol-Gel Sci. Tech.* **2007**, *44*, 41.

(17) Jones, F. R. *J. Adhesion Sci Tech* **2010**, *24*, 171.

(18) Boyle, T. J.; Lambert, T. N.; Pratt, H. D. I.; Lu, P.; Griego, J. J. M.; Bush, N.; Chavez, C. A.; Welk, M. *J. Mater. Sci.* **2010**, *45*, 1744.

(19) Boyle, T. J.; Ottley, L. A. M.; Hoppe, S. M. *Inorg. Chem.* **2010**, *49*, 10798.

(20) Guillet, A. *Macromolecular Symposium* **2003**, *194*, 63.

(21) Kane, M. C.; Londono, J. D.; Beyer, F. L.; Brennan, A. B. *Journal of Applied Crystallography* **2009**, *42*, 925.

(22) Morawetz, H. *Rubber Chemistry and Technology* **2000**, *73*, 405.

(23) Liu, L.; Hu, J.-M.; Leng, W.-H.; Zhang, J.-Q.; Cao, C.-N. *Scripta Materialia* **2007**, *57*, 549.

(24) Zhu, H.; Ma, Z.; Overbury, S. H.; Dai, S. *Cat. Lett.* **2007**, *116*, 128.

(25) Aranguren, M. I. *Encyclopedia of Surface and Colloid Science* **2006**, *2*, 4796.

(26) *American Society of Testing and Materials, ASTM Standards on Building Economics, Fourth Edition*, Philadelphia, PA, 2001., 2001.

(27) *For example, see the publications on the National Institute of Standards and Technology, Building and Fire Research Laboratory website (accessed at* http://www.nist.gov/publication-portal.cfm?defaultSearch=false&q=&authorlist=&researchfield=155&seriesName=&datefrom=&dateto= *on December 5, 2010) for a list of the types of analysis to which this Standards document has been applied.*

(28) Ehlen, M. A. *J. Infrastructure Systems* **1997**, *3*.

(29) *Performance requirements are the set of functional tasks that the asset or set of assets must meet. They are intended to be generic or abstract enough that alternate, competing*

strategies can be considered and compared. Prescriptive requirements, in contrast, are requirements that often prescribe specific techniques or technologies.

(30) *E.g., see The Washington Post, "Beacon Power declares bankruptcy; second loan guarantee recipient to falter," accessed at* http://www.washingtonpost.com/national/health-science/beacon-power-declares-bankruptcy-second-loan-guarantee-recipient-to-falter/2011/10/31/gIQACNAaaM_story.html *on August 2, 2012.*

(31) *Boston Business Journal (* http://www.bizjournals.com/boston/news/2011/08/09/beacon-power-revenue-triples-in-q2.html *)* **August 9, 2011,**.

(32) http://www.power-thru.com/energy_utility.html

(33) *EPRI, Electric Energy Storage Technology Options: A White Paper Primer on Applications, Costs, and Benefits, Report 1020676; Table 3*, December 2010.

DISTRIBUTION

1	MS0958	Ben Anderson	01835
1	MS0958	William Miller	01833
1	MS1137	Mark Ehlen	06924
1	MS1349	Timothy Boyle	01815
1	MS1349	William Hammetter	01815
1	MS1411	Nelson Bell	01816
1	MS0899	Technical Library	9536 (electronic copy)


Sandia National Laboratories